Chapter 10
Constitutive Equations of Metals

The plasticity theory has highly developed through the prediction of deformation of metals up to date. The reason would be caused by the fact that, among various materials exhibiting plastic deformation, metals are used most widely as engineering materials and exhibit the simplest plastic deformation behavior without a pressure dependence, a plastic compressibility, a dependence on the third invariant of deviatoric stress and a softening. Nevertheless, metals exhibit various particular aspects, e.g., the kinematic hardening and the stagnation of isotropic hardening in a cyclic loading. Explicit constitutive equations of metals will be delineated in this chapter, which are based on the extended subloading surface model described in the preceding chapters.

10.1 Isotropic and Kinematic Hardening

The yield function for the Mises yield condition is extended to incorporate kinematic hardening by replacing $\boldsymbol{\sigma}'$ to $\hat{\boldsymbol{\sigma}}'$ in Eqs. (6.55), (6.58) and (9.50) as follows:

$$f(\hat{\boldsymbol{\sigma}}) = \sqrt{\frac{3}{2}}\|\hat{\boldsymbol{\sigma}}'\|, \ \hat{\mathbf{n}} = \hat{\mathbf{n}}' = \bar{\mathbf{n}}' = \frac{\hat{\boldsymbol{\sigma}}'}{\|\hat{\boldsymbol{\sigma}}'\|} \tag{10.1}$$

while the subloading function $f(\overline{\boldsymbol{\sigma}})$ for Eq. (10.1) is given by

$$\boxed{f(\overline{\boldsymbol{\sigma}}) = \sqrt{\frac{3}{2}}\|\overline{\boldsymbol{\sigma}}'\|}, \ \bar{\mathbf{n}} = \bar{\mathbf{n}}' = \bar{\mathbf{n}}' = \frac{\overline{\boldsymbol{\sigma}}'}{\|\overline{\boldsymbol{\sigma}}'\|} \tag{10.2}$$

Further, the elastic-core function in Eq. (9.12) for Eq. (10.1) is given by

K. Hashiguchi, *Foundations of Elastoplasticity: Subloading Surface Model*,
DOI 10.1007/978-3-319-48821-9_10

$$\boxed{f(\hat{\mathbf{c}}) = \sqrt{\frac{3}{2}}\|\hat{\mathbf{c}}'\|}, \quad \frac{\partial f(\hat{\mathbf{c}})}{\partial \hat{\mathbf{c}}} = \sqrt{\frac{3}{2}}\frac{\mathbf{c}'}{\|\hat{\mathbf{c}}'\|} \tag{10.3}$$

It follows from Eq. (9.12) with Eq. (10.3) that

$$\boxed{\mathfrak{R}_c = \sqrt{\frac{3}{2}}\frac{\|\hat{\mathbf{c}}'\|}{F}}, \quad \hat{\mathbf{n}}_c = \frac{\hat{\mathbf{c}}'}{\|\hat{\mathbf{c}}'\|} \tag{10.4}$$

The isotropic hardening function is given by Eq. (6.56), i.e.

$$\boxed{F(H) = F_0\{1 + h_1[1 - \exp(-h_2 H)]\}}, \quad F' = F_0 h_1 h_2 \exp(-h_2 H) \tag{10.5}$$

$$\dot{H} = \sqrt{\frac{2}{3}}||\mathbf{d}^p|| = \dot{\bar{\lambda}} f_{Hn}(\boldsymbol{\sigma}, H; \bar{\mathbf{n}}) \tag{10.6}$$

$$f_{Hn}(\boldsymbol{\sigma}, H; \bar{\mathbf{n}}) = \sqrt{\frac{2}{3}} \tag{10.7}$$

where F_0, h_1, h_2 are the material constants. The hardening function F in Eq. (10.7) increases from the initial value F_0 by the equivalent plastic strain ε^{eqp} and saturates when it reaches the maximum value $(1 + h_1)F_0$ as shown in Fig. 10.1.

Let the following evolution rule of the nonlinear kinematic hardening based on Eq. (6.103) be given for metals as follows:

$$\boxed{\mathring{\boldsymbol{\alpha}} = c_k\left(\mathbf{d}^p - \frac{1}{\sqrt{3/2}\zeta F}||\mathbf{d}^p||\boldsymbol{\alpha}\right) = \dot{\bar{\lambda}}\,\bar{\mathbf{f}}_{kn}(\boldsymbol{\sigma}, \boldsymbol{\alpha}; \bar{\mathbf{n}})} \tag{10.8}$$

$$\bar{\mathbf{f}}_{kn}(\boldsymbol{\sigma}, \boldsymbol{\alpha}; \bar{\mathbf{n}}) = c_k\left(\bar{\mathbf{n}} - \frac{1}{\sqrt{3/2}\zeta F}\boldsymbol{\alpha}\right) \tag{10.9}$$

where ζ is the material constant. As shown in Fig. 10.2, $\boldsymbol{\alpha}$ translates toward the conjugate point, i.e. $\boldsymbol{\alpha} \to \sqrt{3/2}\zeta F\overline{\boldsymbol{\sigma}}'/||\overline{\boldsymbol{\sigma}}'||$ on the limit surface $\|\boldsymbol{\alpha}\| = \sqrt{3/2}\zeta F$ of kinematic hardening.

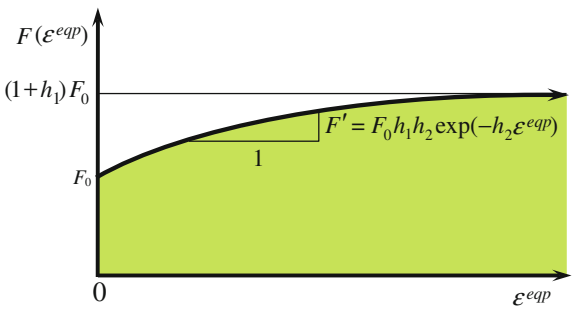

Fig. 10.1 Isotropic hardening function in the uniaxial loading process

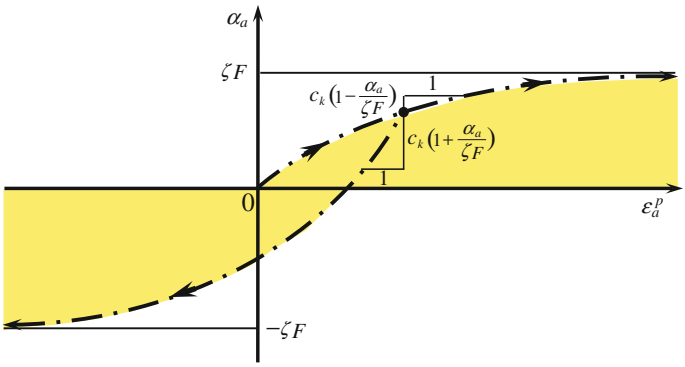

Fig. 10.2 Kinematic hardening rule illustrated for uniaxial loading process

The following relation holds in the uniaxial loading process ($\alpha_a = \sqrt{2/3}\,\|\boldsymbol{\alpha}\|, \varepsilon_a^p = \sqrt{2/3}\,\|\boldsymbol{\varepsilon}^p\|$) from Eq. (10.8).

$$\dot{\alpha}_a = c_k\left(\dot{\varepsilon}_a^p - \frac{\alpha_a}{\zeta F}\left|\dot{\varepsilon}_a^p\right|\right) = c_k\left(1 \mp \frac{\alpha_a}{\zeta F}\right)\dot{\varepsilon}_a^p \left(\text{upper} : \dot{\varepsilon}_a^p > 0, \text{lower} : \dot{\varepsilon}_a^p < 0\right) \tag{10.10}$$

which is time-integrated for $F=$ const. as follows:

$$\frac{\zeta F - \alpha_a}{\zeta F - \alpha_{a0}} = \exp\left[\mp \frac{c_k}{\zeta F}\left(\varepsilon_a^p - \varepsilon_{a0}^p\right)\right] \tag{10.11}$$

where α_{a0} is the initial value of α_a. The relation of α_a versus ε_a^p is shown in Fig. 10.2. The axial back stress saturates at $\alpha_a = \alpha'_a = \zeta F$. Here, it should be noted that the saturation value of the axial stress is not $\sigma_a = (1+\zeta)F$ but it is given by $\sigma_a = [1 + (3/2)\zeta]F$, substituting $\hat{\sigma}'_a = \alpha'_a - \alpha'_a = (2/3)\sigma_a - \zeta F$ into $\hat{\sigma}^{eq} = \sqrt{3/2}||\hat{\boldsymbol{\sigma}}'|| = (3/2)\hat{\sigma}'_a = F$.

The plastic modulus is given by substituting Eqs. (9.16), (10.2), (10.3), (10.7) and (10.9) into Eq. (9.39) as follows:

$$\boxed{\bar{M}^p \equiv \frac{\overline{\boldsymbol{\sigma}}'}{\|\overline{\boldsymbol{\sigma}}'\|} : \left[\sqrt{\frac{2}{3}}\frac{F'}{F}\overline{\boldsymbol{\sigma}} + c_k R\left(\frac{\overline{\boldsymbol{\sigma}}'}{\|\overline{\boldsymbol{\sigma}}'\|} - \frac{1}{\sqrt{3/2}\zeta F}\boldsymbol{\alpha}\right) + c(1-R)\left(\frac{\overline{\boldsymbol{\sigma}}'}{\|\overline{\boldsymbol{\sigma}}'\|} - \frac{\Re_c}{\xi}\frac{\hat{\mathbf{c}}'}{\|\hat{\mathbf{c}}'\|}\right) + \frac{U}{R}\widetilde{\boldsymbol{\sigma}}\right]}$$

$$= \frac{2}{3}RF' + c_k R\left(1 - \frac{1}{\sqrt{3/2}3\zeta F}\frac{\overline{\boldsymbol{\sigma}}'}{\|\overline{\boldsymbol{\sigma}}'\|} : \boldsymbol{\alpha}\right) + c(1-R)\left(1 - \frac{\Re_c}{\xi}\frac{\overline{\boldsymbol{\sigma}}'}{\|\overline{\boldsymbol{\sigma}}'\|} : \frac{\hat{\mathbf{c}}'}{\|\hat{\mathbf{c}}'\|}\right) + \frac{U}{R}\frac{\overline{\boldsymbol{\sigma}}'}{\|\overline{\boldsymbol{\sigma}}'\|} : \widetilde{\boldsymbol{\sigma}} \tag{10.12}$$

10.2 Cyclic Stagnation of Isotropic Hardening

It is observed through experiments for metals that the isotropic hardening stagnates and only the kinematic hardening proceeds in a certain period of reverse deformation starting from the reverse re-yielding. This phenomenon considerably affects the cyclic loading behavior in which the reverse loading is repeated. To describe this phenomenon, the concept of the *cyclic stagnation of isotropic hardening*, i.e. *nonhardening region* was proposed by Chaboche et al. (1979; see also Chaboche 1989) and studied also by Ohno (1982). The concept insists that isotropic hardening does not proceed when the plastic strain given by the time-integration of plastic strain rate lies inside a certain region, called the *nonhardening region*, in the plastic strain space. The non-hardening region expands and translates when the plastic strain lies on the boundary of the region and the plastic strain rate is induced directing outwards the region. It is similar to the notion of the yield surface based on the assumption that the plastic strain rate is induced only when the stress lies on that surface, while the plastic strain and the rate of isotropic hardening variable for the nonhardening region correspond to the stress and the plastic strain rate, respectively, for the yield surface. Thereafter, the other formulation that the isotropic hardening stagnates when the back stress lies inside the certain region of stress space was proposed by Yoshida and Uemori (2002, 2003), where the nonlinear kinematic hardening rule is adopted. Here, it should be noted that the time-integration of the plastic strain rate has no physical meaning in a general state under a material rotation, so that it is not a state variable, and the formulation of the isotropic hardening stagnation in terms of the time-integration of the plastic strain rate cannot be unified as a stress space formulation (cannot be depicted in the stress space). In contrast, the back stress is obviously the state variable and the isotropic hardening stagnation in terms of the back stress can be unified as a stress space formulation. Then, the rigorous formulation for the isotropic hardening stagnation was provided based on the notion of the subloading surface model by Hashiguchi (2015c), adopting the back stress instead of the plastic strain following Yoshida and Uemori (2002, 2003), as will be described in this section.

Assuming that the isotropic hardening stagnates when the back stress $\boldsymbol{\alpha}$ lies inside a certain region, let the following surface, called the *normal-isotropic hardening surface*, be introduced.

$$\mathrm{g}(\widetilde{\boldsymbol{\alpha}}) = \widetilde{K} \tag{10.13}$$

where

$$\widetilde{\boldsymbol{\alpha}} \equiv \boldsymbol{\alpha} - \boldsymbol{\rho} \tag{10.14}$$

$\widetilde{K}$ and $\boldsymbol{\rho}\,(=\boldsymbol{\rho}')$ designate the size and the center, respectively, of the normal-isotropic hardening surface, the evolution rules of which will be formulated later. Furthermore, we introduce the surface, called the *subloading-isotropic hardening surface*, which always passes through the current back stress $\boldsymbol{\alpha}$ and which has a similar shape and an orientation to the normal-isotropic hardening surface (see Fig. 10.3). It is expressed by the following equation.

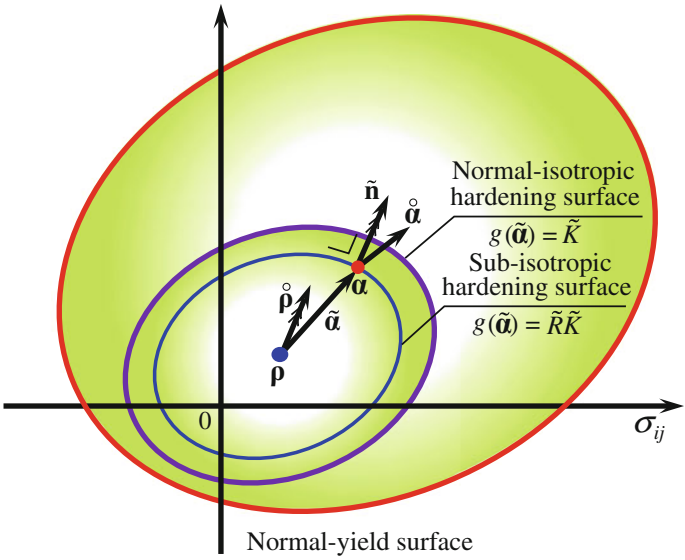

(a) General case

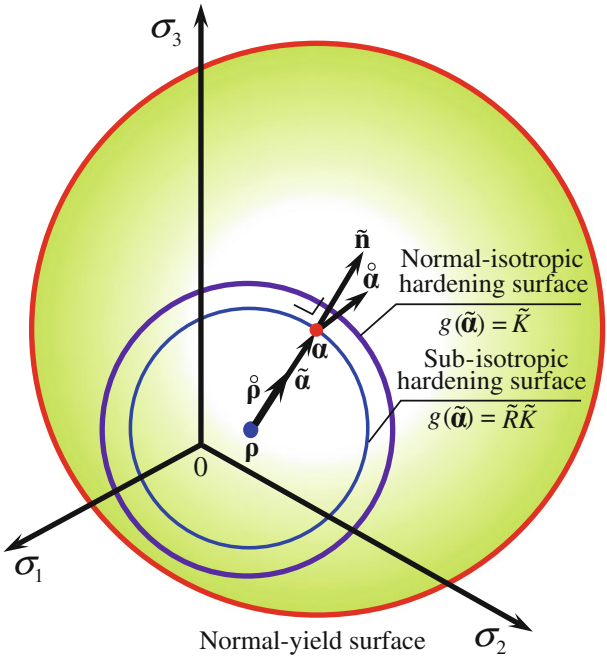

(b) Mises metals

Fig. 10.3 Normal- and sub-isotropic hardening surfaces

$$\boxed{\mathrm{g}(\widetilde{\boldsymbol{\alpha}}) = \widetilde{R}\widetilde{\mathrm{K}}} \tag{10.15}$$

where $\widetilde{R}(0 \leq \widetilde{R} \leq 1)$ is the ratio of the size of subloading-isotropic hardening surface to that of the normal-isotropic hardening surface. It plays the role as the measure for the approaching degree of the back stress to the normal-isotropic hardening surface. Then, $\widetilde{R}$ is referred to as the *normal-isotropic hardening ratio*. It is calculable from the equation $\widetilde{R} = \mathrm{g}(\widetilde{\boldsymbol{\alpha}})/\widetilde{\mathrm{K}}$ in terms of the known values $\boldsymbol{\alpha}$, $\boldsymbol{\rho}$ and $\widetilde{K}$.

The consistency condition of the sub-isotropic hardening surface is given by

$$\frac{\partial \mathrm{g}(\widetilde{\boldsymbol{\alpha}})}{\partial \widetilde{\boldsymbol{\alpha}}} : \mathring{\boldsymbol{\alpha}} - \frac{\partial \mathrm{g}(\widetilde{\boldsymbol{\alpha}})}{\partial \widetilde{\boldsymbol{\alpha}}} : \mathring{\boldsymbol{\rho}} = \dot{\widetilde{R}}\widetilde{K} + \widetilde{R}\dot{\widetilde{K}}. \tag{10.16}$$

Let the following postulates be adopted for the formulations of the evolution rules of $\widetilde{K}$ and $\boldsymbol{\rho}$.

(1) $\widetilde{K}$ and $\boldsymbol{\rho}$ evolve when the back stress rate $\mathring{\boldsymbol{\alpha}}$ is induced directing outwards the subloading-isotropic hardening surface, fulfilling

$$\frac{\partial \mathrm{g}(\widetilde{\boldsymbol{\alpha}})}{\partial \widetilde{\boldsymbol{\alpha}}} : \mathring{\boldsymbol{\alpha}} > 0 \tag{10.17}$$

(2) The rates of $\widetilde{K}$ and $\boldsymbol{\rho}$ increase as the back stress approaches the normal-isotropic hardening surface, i.e. as the normal-isotropic hardening ratio $\widetilde{R}$ increases. Therefore, they are monotonic-increasing function of the normal-isotropic hardening ratio $\widetilde{R}$.

(3) The back stress $\boldsymbol{\alpha}$ is assumed to exist inside the normal-isotropic hardening surface. Therefore, it must hold that

$$\dot{\widetilde{R}} = 0 \text{ for } \widetilde{R} = 1 \tag{10.18}$$

(4) The consistency condition in Eq. (10.16) reduces to the following relation which must be fulfilled when the back stress just lies on the normal-isotropic hardening surface.

$$\frac{\partial \mathrm{g}(\widetilde{\boldsymbol{\alpha}})}{\partial \widetilde{\boldsymbol{\alpha}}} : \mathring{\boldsymbol{\alpha}} - \frac{\partial \mathrm{g}(\widetilde{\boldsymbol{\alpha}})}{\partial \widetilde{\boldsymbol{\alpha}}} : \mathring{\boldsymbol{\rho}} = \dot{\widetilde{K}} \text{ for } \widetilde{R} = 1. \tag{10.19}$$

Then, we assume the following equations so as to fulfill all these postulates.

$$\boxed{\dot{\widetilde{K}} = C\widetilde{R}^{\zeta}\langle \widetilde{\mathbf{n}} : \mathring{\boldsymbol{\alpha}} \rangle \left\| \frac{\partial \mathrm{g}(\widetilde{\boldsymbol{\alpha}})}{\partial \widetilde{\boldsymbol{\alpha}}} \right\|}, \tag{10.20}$$

$$\boxed{\mathring{\boldsymbol{\rho}} = (1-C)\widetilde{R}^{\varsigma}\langle \widetilde{\mathbf{n}} : \mathring{\boldsymbol{\alpha}} \rangle \widetilde{\mathbf{n}}}, \tag{10.21}$$

where $0 \leq C \leq 1$ and $\varsigma(\geq 1)$ are the material constants and

$$\widetilde{\mathbf{n}} \equiv \frac{\partial \mathrm{g}(\widetilde{\boldsymbol{\alpha}})}{\partial \widetilde{\boldsymbol{\alpha}}} \Big/ \left\| \frac{\partial \mathrm{g}(\widetilde{\boldsymbol{\alpha}})}{\partial \widetilde{\boldsymbol{\alpha}}} \right\|. \tag{10.22}$$

Substituting Eqs. (10.21) and (10.22) for the evolution rules of $\widetilde{K}$ and $\boldsymbol{\rho}$ into Eq. (10.17), the rate of the normal-isotropic hardening ratio is given by

$$\begin{aligned} \mathring{\widetilde{R}} &= \frac{1}{\widetilde{K}} \left[\left\langle \frac{\partial \mathrm{g}(\widetilde{\boldsymbol{\alpha}})}{\partial \widetilde{\boldsymbol{\alpha}}} : \mathring{\boldsymbol{\alpha}} \right\rangle - (1-C)\widetilde{R}^{\varsigma} \frac{\partial \mathrm{g}(\widetilde{\boldsymbol{\alpha}})}{\partial \widetilde{\boldsymbol{\alpha}}} : \langle \widetilde{\mathbf{n}} : \mathring{\boldsymbol{\alpha}} \rangle \widetilde{\mathbf{n}} - \widetilde{R} C \widetilde{R}^{\varsigma} \langle \widetilde{\mathbf{n}} : \mathring{\boldsymbol{\alpha}} \rangle \left\| \frac{\partial \mathrm{g}(\widetilde{\boldsymbol{\alpha}})}{\partial \widetilde{\boldsymbol{\alpha}}} \right\| \right] \\ &= \frac{1}{\widetilde{K}} \left\langle \frac{\partial \mathrm{g}(\widetilde{\boldsymbol{\alpha}})}{\partial \widetilde{\boldsymbol{\alpha}}} : \mathring{\boldsymbol{\alpha}} \right\rangle \{1 - [1 - C(1 - \widetilde{R})]\widetilde{R}^{\varsigma}\} \end{aligned} \tag{10.23}$$

which is the monotonically-decreasing function of $\widetilde{R}$ fulfilling

$$\mathring{\widetilde{R}} \begin{cases} = \dfrac{1}{\widetilde{K}} \left\langle \dfrac{\partial \mathrm{g}(\widetilde{\boldsymbol{\alpha}})}{\partial \widetilde{\boldsymbol{\alpha}}} : \mathring{\boldsymbol{\alpha}} \right\rangle (>0) & \text{for} \quad \widetilde{R} = 0 \\ < \dfrac{1}{\widetilde{K}} \left\langle \dfrac{\partial \mathrm{g}(\widetilde{\boldsymbol{\alpha}})}{\partial \widetilde{\boldsymbol{\alpha}}} : \mathring{\boldsymbol{\alpha}} \right\rangle (>0) & \text{for} \quad \widetilde{R} < 1 \\ = 0 \text{ for } \widetilde{R} = 1 \\ < 0 \text{ for } \widetilde{R} > 1 \end{cases} \tag{10.24}$$

as shown in Fig. 10.4. Therefore, the normal-isotropic hardening ratio increases when the back stress moves to the outward of the sub-isotropic hardening surface

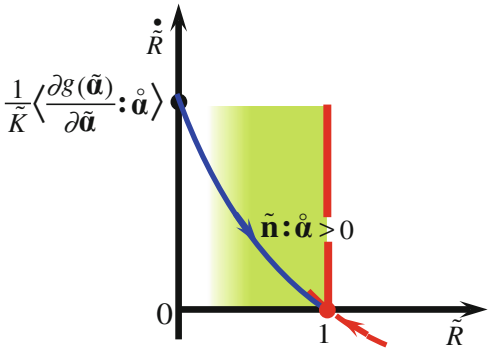

Fig. 10.4 Evolution of normal-isotropic hardening ratio: back stress is attracted to the normal-isotropic hardening surface

but it decreases such that the normal-isotropic hardening surface involves the back stress when the back stress goes out from the normal-isotropic hardening surface by virtue of the inequality $\dot{\widetilde{R}} < 0$ for $\widetilde{R} > 1$ as shown in Eq. (10.24). Furthermore, needless to say, the judgment of whether the back stress reaches the normal-isotropic hardening surface is not necessary in the present formulation.

It is assumed that the isotropic hardening variable H evolves under the following conditions.

(1) The isotropic hardening is induced when the back stress rate $\mathring{\boldsymbol{\alpha}}$ is induced directing outwards the sub-isotropic hardening surface, i.e.

$$\dot{H}\begin{cases} > 0 & \text{for } \widetilde{\mathbf{n}} : \mathring{\boldsymbol{\alpha}} > 0 \\ = 0 & \text{for } \widetilde{\mathbf{n}} : \mathring{\boldsymbol{\alpha}} \leq 0 \end{cases} \tag{10.25}$$

(2) The isotropic hardening rate increases as the back stress approaches the normal-isotropic hardening surface, i.e. as the normal-isotropic hardening ratio $\widetilde{R}$ increases. Then, $\dot{H}$ is the monotonically-increasing function of $\widetilde{R}$. Here, in order that the isotropic hardening develops continuously, its rate must be zero, i.e. $\dot{H} = 0$ for $\widetilde{R} = 0$, i.e. when the back stress lies just on the center of the normal-isotropic hardening surface because the rate is zero during the process in which the back stress moves towards the inside of the sub-isotropic stagnation surface.

(3) The isotropic hardening rule of Eq. (10.6) in the monotonic loading process holds when the back stress lies on the normal-isotropic hardening surface $(\widetilde{R} = 1)$ and the plastic strain rate is induced in the outward-direction of that surface.

Eventually, let the following evolution rule of isotropic hardening be assumed by extending Eq. (10.6).

$$\boxed{\dot{H} = \sqrt{\frac{2}{3}}\widetilde{R}^{\upsilon}\langle \widetilde{\mathbf{n}} : \overline{\mathbf{n}}_{kn} \rangle ||\mathbf{d}^p||} \tag{10.26}$$

where υ is the material constant and $\overline{\mathbf{n}}_{kn}$ is the normalized direction of increment of the back stress, noting Eq. (10.9).

$$\overline{\mathbf{n}}_{kn} \equiv \frac{\overline{\mathbf{f}}_{kn}}{||\overline{\mathbf{f}}_{kn}||} \tag{10.27}$$

Employing the extended isotropic hardening rule in Eq. (10.27) instead of Eq. (10.7) into Eq. (10.12), the plastic modulus is modified as follows:

$$\boxed{\bar{M}^p \equiv \bar{\mathbf{n}} : \left[\sqrt{\frac{2}{3}}\frac{F'}{F}\widetilde{R}\langle \widetilde{\mathbf{n}} : \overline{\mathbf{n}}_{kn} \rangle \overline{\boldsymbol{\sigma}} + R\overline{\mathbf{f}}_{kn} + \frac{U}{R}\widetilde{\boldsymbol{\sigma}} + (1 - R)\overline{\mathbf{f}}_{cn} \right]} \tag{10.28}$$

The normal-isotropic hardening surface evolves such that the boundary of the surface always approaches the back stress and moves so as to involve it even if the back stress goes out from the boundary by the inequality $\dot{\widetilde{R}} < 0$ for $\widetilde{R} > 1$ as shown in Eq. (10.24). Furthermore, the judgment of whether the back stress reaches the normal-isotropic hardening surface is not necessary in the present formulation. In contrast, the judgment whether the plastic strain or the back stress reaches the isotropic hardening (stagnation) surface is required in the other models (Chaboche et al. 1979; Chaboche 1991; Ohno 1982; Yoshida and Uemori 2002). In addition, the boundary of the isotropic (stagnation) surface does not approach the plastic strain or the back stress and does not move so as to involve it even if they go out from the surface. Therefore, these models would be obliged to abandon the incorporation of isotropic stagnation (Chaboche 2008; Kobayashi and Ohno 2002) except for the calculation by the forward-Euler method with infinitesimal loading increments, although the isotropic stagnation formulations have been proposed by the proposers of these cyclic kinematic models themselves.

The function $g(\widetilde{\boldsymbol{\alpha}})$ is given in the simplest form as follows:

$$g(\widetilde{\boldsymbol{\alpha}}) = \|\widetilde{\boldsymbol{\alpha}}\|, \quad \tilde{\mathbf{n}} = \frac{\tilde{\boldsymbol{\alpha}}}{||\tilde{\boldsymbol{\alpha}}||}, ||\frac{\partial g(\tilde{\boldsymbol{\alpha}})}{\partial \tilde{\boldsymbol{\alpha}}}|| = ||\tilde{\mathbf{n}}|| = 1 \tag{10.29}$$

which will be used in the subsequent sections for the comparisons with test data. It follows from Eq. (10.28) that

10.3 Calculation of Normal-Yield Ratio

The normal-yield ratio R must be calculated from the equation of the subloading surface in the unloading process ($\mathbf{d}^p = \mathbf{O}$). It can be calculated directly by $R = f(\hat{\boldsymbol{\sigma}})/F$ in the initial subloading surface model. However, it has to be calculated by solving the equation of the subloading surface in the extended subloading surface model as described below.

Substituting Eq. (9.6) into Eq. (10.2), the extended subloading surface is described as follows:

$$\sqrt{\frac{3}{2}}\|\widetilde{\boldsymbol{\sigma}}' + R\hat{\mathbf{c}}'\| = RF(H) \tag{10.30}$$

i.e.

$$\mathrm{tr}\,(\widetilde{\boldsymbol{\sigma}}' + R\hat{\mathbf{c}}')^2 = \frac{2}{3}R^2F^2 \tag{10.31}$$

The normal-yield ratio R is derived from the quadratic Eq. (10.31) as follows:

$$R = \frac{\widetilde{\boldsymbol{\sigma}}' : \hat{\mathbf{c}}' + \sqrt{(\widetilde{\boldsymbol{\sigma}}' : \hat{\mathbf{c}}')^2 + \left(\frac{2}{3}F^2 - \left\|\hat{\mathbf{c}}'\right\|^2\right)\left\|\widetilde{\boldsymbol{\sigma}}'\right\|^2}}{\frac{2}{3}F^2 - \left\|\hat{\mathbf{c}}'\right\|^2} \tag{10.32}$$

10.4 Material Parameters and Comparisons with Test Data

Material parameters will be collectively shown and the capability of the subloading surface model to describe various loading behavior will be verified by the comparisons with test data in this section.

10.4.1 Material Parameters

Material parameters are shown collectively below for three versions of the subloading surface model. Eqs. (7.20) and (7.62) will be used as the functions in the evolution equation of the normal-yield ratio and the tangential-inelastic strain rate in the following.

i) The simplest subloading surface model, which is the improvement of the conventional elastoplasticity model only with the isotropic and the kinematic hardenings, contains the following 7 material constants and 2 initial values.

Material constants:

Elastic moduli: E, ν

Hardening $\begin{cases} \text{isotropic: } h_1 \ h_2 \\ \text{kinematic: } c_k, \zeta \end{cases}$

Evolution of normal-yield ratio : u

Initial values:

Normal-yield surface $\begin{cases} \text{size: } F_0 \\ \text{center: } \boldsymbol{\alpha}_0 \end{cases}$

The computer program is shown in **Appendix J** (a) i).

ii) The simplified subloading surface model, in which the tangential-inelastic strain rate and the isotropic hardening stagnation are ignored, contains the following 12 material constants and 3 initial values.

Material constants:

Elastic moduli: E,v

Hardening $\begin{cases} \text{isotropic: } h_1\ h_2 \\ \text{kinematic: } c_k, \zeta \end{cases}$

Evolution of normal-yield ratio : $\bar{u}, u_c, R_e(\geq 1), n(\geq 1)$

Translation of elastic-core: $c,\ \xi(<1)$

Initial values:

Normal-yield surface $\begin{cases} \text{size: } F_0 \\ \text{center: } \boldsymbol{\alpha}_0 \end{cases}$

Elastic-core : $\mathbf{c}_0$

The computer program is shown in **Appendix J** (a) ii).

iii) The most general subloading surface model, which possesses all the behavior involving the tangential-inelastic strain rate and the isotropic stagnation, contains the following 17 material constants and 5 initial values at most, while the full version of computer program is shown in **Appendix J**(a) iii).

Material constants:

Elastic moduli: E,v

Hardening $\begin{cases} \text{isotropic: } h_1\ h_2 \\ \text{kinematic: } c_k, \zeta \end{cases}$

Evolution of normal-yield ratio : $\bar{u}, u_c, R_e(<1), n(\geq 1)$

Translation of elastic-core: $c,\ \xi(<1)$

Tangential inelasticity: $\widetilde{c}(\leq 1), \widetilde{n} = (\geq 1)$

Stagnation of isotropic hardening: $C(0 \leq C \leq 1), \varsigma(>1),\ \upsilon$

Initial values:

Normal-yield surface $\begin{cases} \text{size: } F_0 \\ \text{center: } \boldsymbol{\alpha}_0 \end{cases}$

Elastic-core : $\mathbf{c}_0$

Normal-isotropic hardening surface $\begin{cases} \text{size: } \widetilde{K}_0 \\ \text{center: } \boldsymbol{\rho}_0 \end{cases}$

The computer program is shown in **Appendix J** (a) iii).

The determination of these material parameters is explained below in brief.

(1) Young's modulus E and Poisson's ratio ν are determined from the slope and the ratio of lateral to axial strains in the initial part of stress–strain curve.
(2) h_1, h_2 and F_0 for the isotropic hardening and c_k, ζ and $\boldsymbol{\alpha}_0$ for the kinematic hardening are determined from stress–strain curves in the initial and the inverse loadings.
(3) $\bar{u}$, u_c, $R_e(<1)$ and n for the evolution of the normal-yield ratio are determined from the stress–strain curve in the subyield state, i.e. the elastic-plastic transitional state.
(4) c, ξ and $\mathbf{c}_0$ for the elastic-core are determined from the stress–strain curves in cyclic loading.
(5) $\widetilde{c}$ and $\widetilde{n}$ for the tangential-inelastic strain rate are determined by the difference of the strain in the non-proportional loading from that in the proportional loading.
(6) C, ς, υ, $\widetilde{K}_0$ and $\boldsymbol{\rho}_0$ for the elastic-core are determined from the stress–strain curves in cyclic loading under a constant strain amplitude.

All of these material parameters except for $\widetilde{c}$ and $\widetilde{n}$ for the tangential-inelastic strain rate can be determined only by the stress–strain curves in the uniaxial loading for initial isotropic materials. One can put $\boldsymbol{\alpha}_0 = \mathbf{c}_0 = \boldsymbol{\rho}_0 = \mathbf{O}$ for the initial isotropy, which is assumed in all the subsequent simulations. We may calculate $\widetilde{K}_0$ by $\widetilde{K}_0 = \|\widetilde{\boldsymbol{\alpha}}_0\| (\cong 0)$ leading to $\widetilde{R}_0 = 1$, by input of a small value of $\boldsymbol{\alpha}_0$ and $\boldsymbol{\rho}_0 = \mathbf{O}$ in order that the isotropic hardening rule in Eq. (10.5) with Eq. (10.6) holds in an initial loading process. Tangential inelasticity is irrelevant to the proportional loading.

10.4.2 Comparison with Test Data

The capability of the present model for describing the deformation behavior of metals is verified through comparisons with several basic test data in this section, referring to Hashiguchi et al. (2012) and Hashiguchi and Ueno (2017). Capability of unconventional plasticity model aimed at describing plastic strain rate induced by a rate of stress inside yield surface must be evaluated by a degree in which cyclic loading behavior can be described appropriately. Then, various cyclic loading test data in uniaxial loading are first simulated and thereafter a circular strain path test datum is simulated to verify capability for describing non-proportional loading behavior.

The cyclic loading behavior under the stress amplitude to both positive and negative sides can be predicted to some extent by any models, including even the conventional plasticity model. On the other hand, the prediction of the cyclic loading behavior under the stress amplitude in positive or negative one side, i.e. the pulsating loading inducing the so-called *mechanical ratcheting effect* requires a high ability for the description of plastic strain rate induced by the rate of stress inside the yield surface. Furthermore, it is noteworthy that we often encounter the

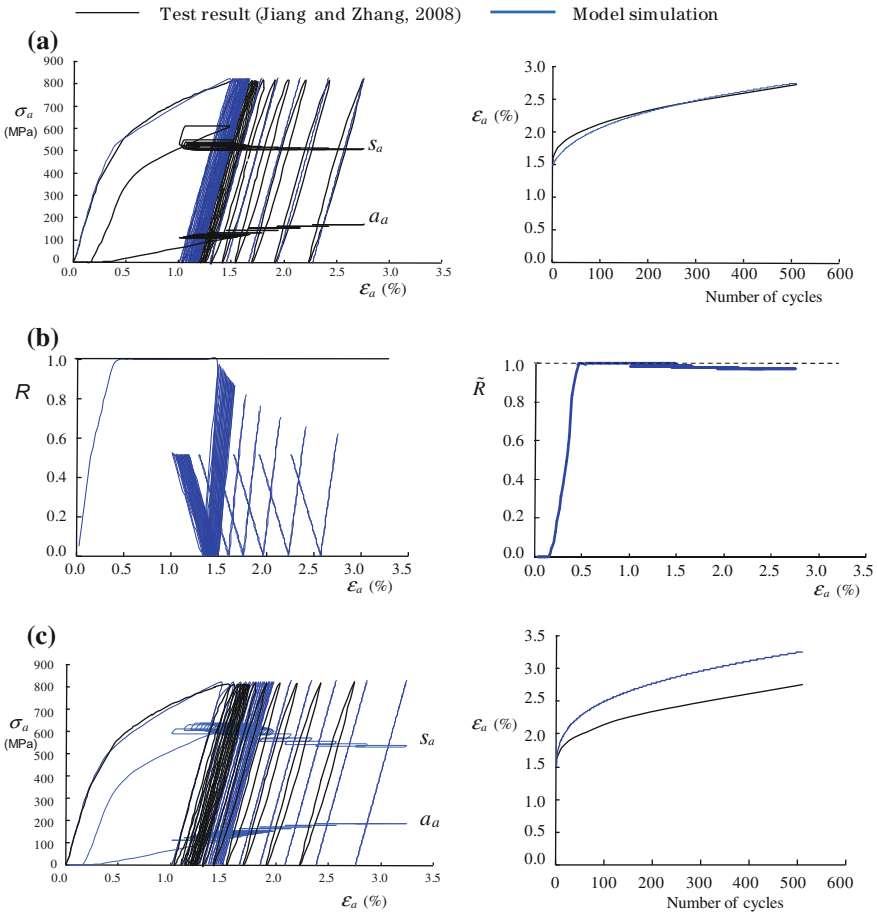

Fig. 10.5 Uniaxial cyclic loading behavior under the pulsating loading between 0 and 830 MPa of 1070 steel (Test data after Jiang and Zhang 2008): **a** Test result and simulation result and simulation without stagnation of isotropic hardening, **b** Variations of normal-yield ratio and normal-isotropic hardening ratio and **c** Test result and simulation without improvement of reloading behavior.

pulsating loading phenomena in the boundary-value problems in engineering practice, e.g. railways and gears. The comparison with the test data for the 1070 steel under the cyclic loading of axial stress between 0 and $+830$ MPa after Jiang and Zhang (2008) is depicted in Fig. 10.5, where the material parameters are selected as follows:

Material constants:

Elastic moduli: $E = 160,000$ MPa, $\nu = 0.3$,

Hardening $\begin{cases} \text{isotropic: } h_1 = 0.58,\ h_2 = 170, \\ \text{kinematic: } c_k = 5000 \text{ MPa}, \zeta = 0.5, \end{cases}$

Evolution of normal-yield ratio: $\bar{u} = 200, u_c = 6, R_e = 0.5, n = 1$,

Translation of elastic-core: $c = 7000$ MPa, $\xi = 0.7$,

Stagnation of isotropic hardening: $C = 0.5, \varsigma = 5, \upsilon = 0.1$,

Initial values:

Isotropic hardening function: $F_0 = 507$ MPa.

The relation of the axial stress and the axial components of back stress and similarity-center versus the axial strain and the relation of the axial strain versus the number of cycles are depicted in Fig. 10.5a, where the axial components are designated by $(\ )_a$. The accumulation of axial strain is simulated closely by the present model. The calculation is controlled automatically such that the stress and the back stress are attracted to the normal-yield and the normal-isotropic hardening surfaces, respectively, as known from the variations of the normal-yield ratio R and the normal-isotropic hardening ratio $\widetilde{R}$ depicted in Fig. 10.5b. Accumulation of axial strain is overestimated as depicted in Fig. 10.5c if the reloading behavior is not improved by setting $u_c = 0$ ignoring the Masing effect. Despite of the improvement for reloading behavior, however, hysteresis loops are simulated as narrower than those in the test result in order to fit the strain accumulation in the test result. A further improvement is desirable for this insufficiency.

Next, examine the uniaxial cyclic loading behavior under the constant stress amplitude to both positive and negative sides with different magnitudes. Comparison with the test data for the 304L steel under the cyclic loading of axial stress between $+250$ and -150 MPa after Hassan et al. (2008) is depicted in Fig. 10.6 where the material parameters are selected as shown below.

Material constants:

Elastic moduli: $E = 200,000$MPa, $\nu = 0.3$,

Hardening $\begin{cases} \text{isotropic: } h_1 = 0.3,\ h_2 = 30, \\ \text{kinematic: } c_k = 130 \text{ MPa}, \zeta = 0.9, \end{cases}$

Evolution of normal-yield ratio: $\bar{u} = 2, u_c = 10, R_e = 0.5, n = 1$,

Translation of elastic-core: $c = 10{,}000$ MPa, $\xi = 0.7$,

Stagnation of isotropic hardening: $C = 0.5, \varsigma = 15, \upsilon = 1$,

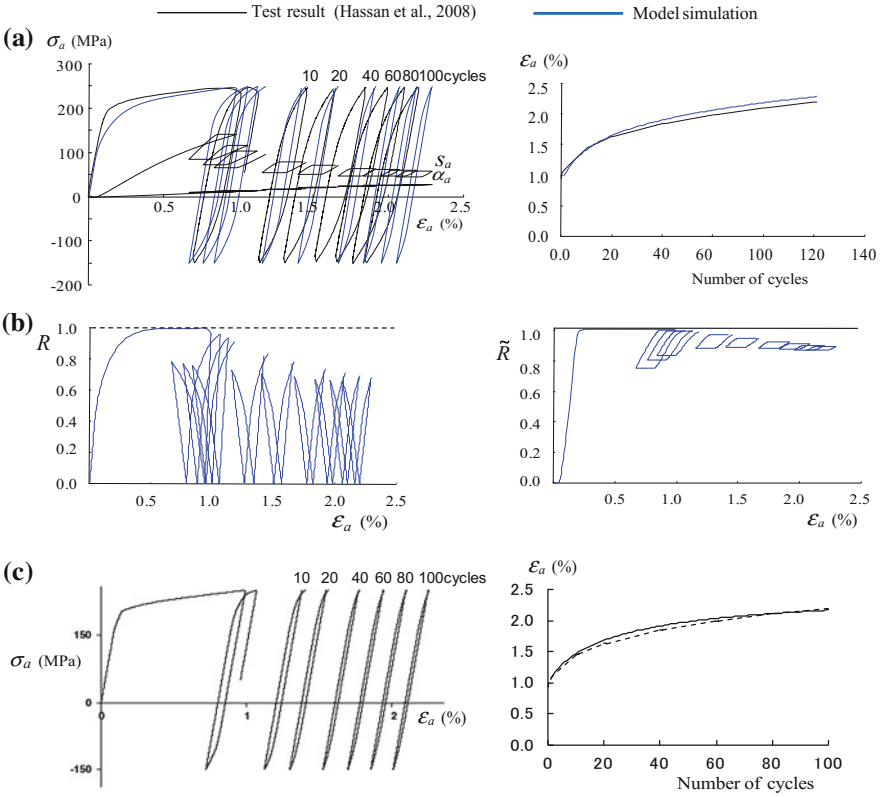

Fig. 10.6 Uniaxial cyclic loading behavior under the constant stress amplitude between −150 and 250 MPa of 304L steel (Test data after Hassan et al. 2008): **a** Test result and simulation, **b** Variations of normal-yield ratio and normal-isotropic hardening ratio and **c** Simulation by modified Chaboche model (cf. Hassan et al. 2008)

Initial values:

Isotropic hardening function: $F_0 = 232$ MPa.

The relation of the axial stress and the axial components of back stress and similarity-center versus the axial strain and the relation of the axial strain versus the number of cycles are depicted in Fig. 10.6a. Both the accumulation of strain and the hysteresis loops are simulated closely by the present model. The calculation is controlled automatically such that the stress and the back stress are attracted to the normal-yield and the normal-isotropic hardening surfaces, respectively, as known from the variations of the normal-yield ratio R and the normal-isotropic hardening ratio $\widetilde{R}$ depicted in Fig. 10.6b. The relations of the axial stress versus the axial strain

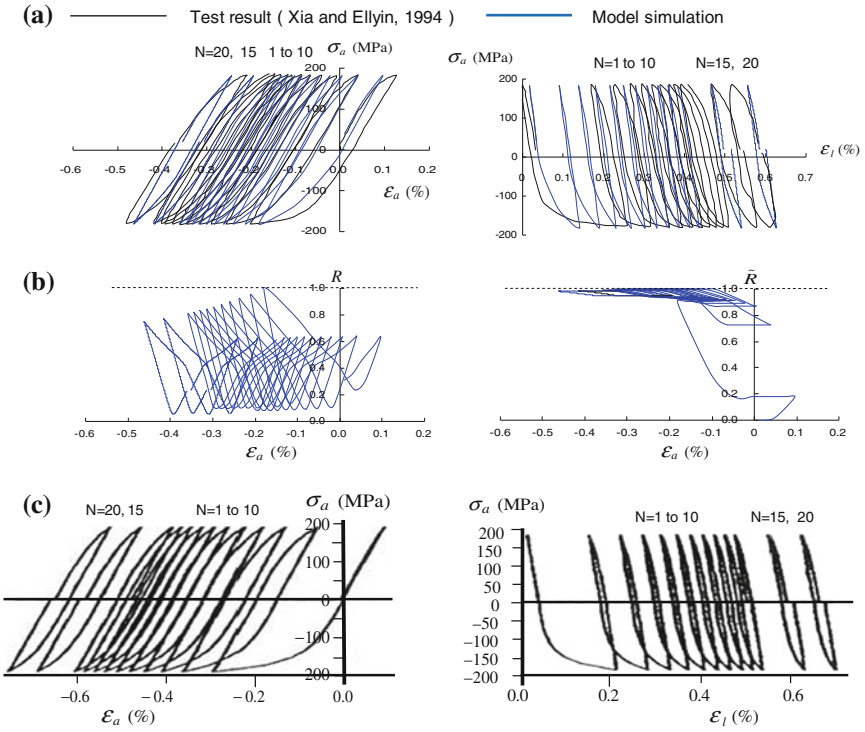

Fig. 10.7 Uniaxial cyclic loading behavior under the constant stress amplitude between −182 and +182 MPa of 304L steel (Test data after Xia and Ellyin 1994): **a** Test result and simulation, **b** Variations of normal-yield ratio and normal-isotropic hardening ratio and **c** Simulation by Xia and Ellyin (1994)

and the relation of the axial strain versus the number of cycles simulated using the modified Chaboche model (Chaboche 1991) are also depicted in Fig. 10.6c in which the strain is simulated as larger than the test result and the hysteresis loops are simulated as narrower than the test data. The prediction of this steel deformation behavior will be improved by incorporating the rate-dependence.

Further, we examine the uniaxial cyclic loading behavior for constant symmetric stress amplitude to both positive and negative sides. Comparison with test data of the 304 steel under the cyclic loading of axial stress between $+182$ and -182 MPa under the constant hoop stress 80 MPa after Xia and Ellyin (1994) is depicted in Fig. 10.7 where the material parameters are selected as follows:

Material constants:

Elastic moduli: $E = 190,000\,\text{MPa},\ \nu = 0.3,$

Hardening $\begin{cases} \text{isotropic: } h_1 = 1.3, h_2 = 100, \\ \text{kinematic: } c_k = 25\ \text{MPa},\ \zeta = 0.3, \end{cases}$

Evolution of normal-yield ratio: $\bar{u} = 200, u_c = 6, R_e = 0.5, n = 1,$

Translation of elastic-core: $c = 5000\ \text{MPa},\ \xi = 0.7,$

Stagnation of isotropic hardening: $C = 0.5, \varsigma = 8, \upsilon = 5,$

Initial values:

Isotropic hardening function: $F_0 = 212\,\text{MPa}.$

The relation of the axial stress and the axial components of back stress and similarity-center versus the axial strain and the circumferential strain ε_l with the number of cycles are shown in Fig. 10.7a, while the back stress is induced quite slightly so that it is invisible in this figure. The simulations for the accumulation of axial strain and the hysteresis loops agree well with the test result, except for the prediction of hysteresis loops as narrower than the test result in the initial stage. Here, the axial strain and the lateral strain are accumulated to the compression side and the extension side, respectively, by the application of the hoop stress 80 MPa. The calculation is automatically controlled such that the stress and the back stress are attracted to the normal-yield and the normal-isotropic hardening surfaces, respectively, as known from the variations of the normal-yield ratio R and the normal-isotropic hardening ratio $\widetilde{R}$ depicted in Fig. 10.7b. The relations of the axial stress versus the axial and lateral strains and the relation with the number of cycles simulated by Xia and Ellyin (1994; cf. also Ellyin 1997) are also depicted in Fig. 10.7c where both the axial and the circumferential strains are overestimated.

Furthermore, examine the uniaxial cyclic loading behavior under the constant symmetric strain amplitudes to both positive and negative sides. Comparison with the test data of the 316 steel under the cyclic loading with the increasing axial strain amplitudes $\pm 1.0, \pm 1.5, \pm 2.0, \pm 2.5, \pm 3.0\,\%$ after Chaboche et al. (1979) is depicted in Fig. 10.8 where the material parameters are selected as follows:

Material constants:

Elastic moduli: $E = 170,000\,\text{MPa},\ \nu = 0.3,$

Hardening $\begin{cases} \text{isotropic: } h_1 = 0.85, h_2 = 5, \\ \text{kinematic: } c_k = 2000\ \text{MPa},\ \zeta = 0.5, \end{cases}$

Evolution of normal-yield ratio: $\bar{u} = 100, u_c = 3, R_e = 0.5, n = 1,$

Translation of elastic-core: $c = 2000\ \text{MPa},\ \xi = 0.7,$

Stagnation of isotropic hardening: $C = 0.5, \varsigma = 5, \upsilon = 1,$

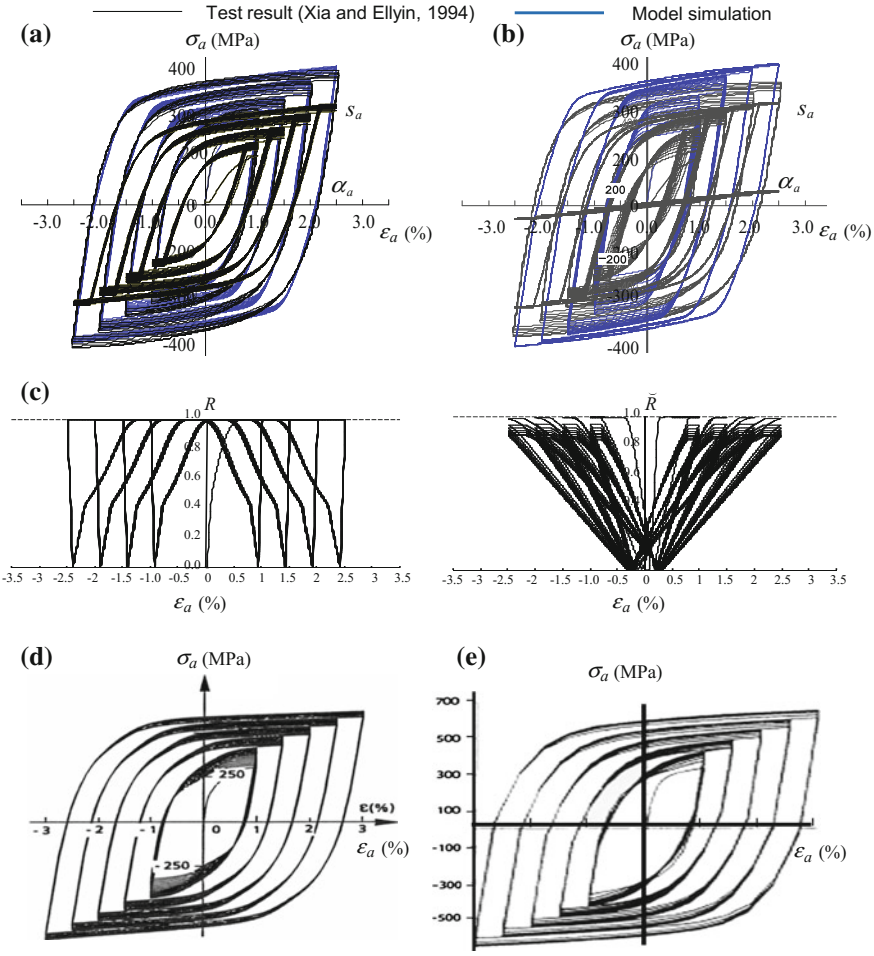

Fig. 10.8 Uniaxial cyclic loading behavior under the constant strain amplitude the 5 levels increasing strain amplitudes of 316 steel (Test data after Chaboche et al. 1979): **a** Test result and simulation by present model, **b** Test result and simulation without stagnation of isotropic hardening, **c** Variations of normal-yield ratio and normal-isotropic hardening, **d** Simulation by Chaboche (2008) and **e** Simulation by Ellyin and Xia (1989)

Initial values:

Isotropic hardening function: $F_0 = 320\,\text{MPa}$.

The relation of the axial stress and the axial components of back stress and similarity-center versus the axial strain are shown in Fig. 10.8a. The hysteresis loops and the stagnation of isotropic hardening are simulated closely by the present model. On the other hand, the calculated result without the cyclic stagnation of

isotropic hardening overestimates the hardening behavior as shown in Fig. 10.8b. The calculation is controlled automatically such that the stress and the back stress are attracted to the normal-yield and the normal-isotropic hardening surfaces, respectively, as known from the variations of the normal-yield ratio R and the normal-isotropic hardening ratio $\widetilde{R}$ depicted in Fig. 10.8c. The relations of the axial stress and the axial strain simulated by Chaboche (1991) and Ellyin and Xia (1989) are depicted in Fig. 10.8d, e, respectively. The strain in the initial stage is simulated as larger than the test result by the former and the curves predicted by the latter is not smooth but piece-wise linear.

Finally, we examine the non-proportional loading behavior. Comparison with the test data of the austenitic 17–12 Mo SPH carbon stainless steel subjected to the approximately circular strain path in the strain plane $(\varepsilon_a, \varepsilon_{a\theta})$ by the inputs of the axial strain $\varepsilon_a = 0.004\sin(\alpha - \pi/2)$ and the axial-circumferential shear strain $\varepsilon_{a\theta} = 0.0036\sin\alpha$ in the sinusoidal waves under the constant circumferential normal stress σ_θ = 50 MPa during 40 cycles after the uniaxial loading to $\varepsilon_a = 0.004$ after Delobelle et al. (1995) is depicted in Fig. 10.9. Here, α is the angle measured from the axis of ε_a in the strain plane $(\varepsilon_a, \varepsilon_{a\theta})$. Consequently, the cyclic loadings of the axial strain ε_a under the constant amplitude $\varepsilon_a = \pm 0.004$ and of the axial-circumferential shear strain $\varepsilon_{a\theta}$ under the constant amplitude $\varepsilon_{a\theta} = \pm 0.0036$ are executed simultaneously, while the phase of $\varepsilon_{a\theta}$ is later than that of ε_a by $\pi/2$. The material parameters are selected as follows:

Material constants:

Elastic moduli: $E = 170,000$ MPa, $\nu = 0.3$ (G = 65,385 MPa),

Hardening $\begin{cases} \text{isotropic: } h_1 = 1.7, h_2 = 40, \\ \text{kinematic: } c_k = 200 \text{ MPa}, \ \zeta = 0.9, \end{cases}$

Evolution of normal-yield ratio: $\bar{u} = 800, u_c = 3, R_e = 0.5, n = 1$,

Translation of elastic - core: c = 7000 MPa, $\xi = 0.7$,

Tangential inelasticity: $\widetilde{c} = 0.6$, $\widetilde{n} = 3$,

Stagnation of isotropic hardening: $C = 0.5, \varsigma = 5, \upsilon = 1$,

Initial values:

Isotropic hardening function: $F_0 = 240$ MPa.

The strain path $(\varepsilon_a, \varepsilon_\theta)$ (ε_θ: circumferential normal strain) and the stress path $(\sigma_a, \sqrt{3}\sigma_{a\theta})$ ($\sigma_{a\theta}$: axial-circumferential shear stress) are shown for the test result and the model simulation in Fig. 10.9a, b, respectively. The simulation of the stress path and the accumulation of lateral strain are in good agreement with the test result. The stress and the back stress are attracted to the normal-yield and the normal-isotropic hardening surfaces, respectively, as known from the variations of the normal-yield ratio R and the normal-isotropic hardening ratio $\widetilde{R}$ depicted in Fig. 10.9b.

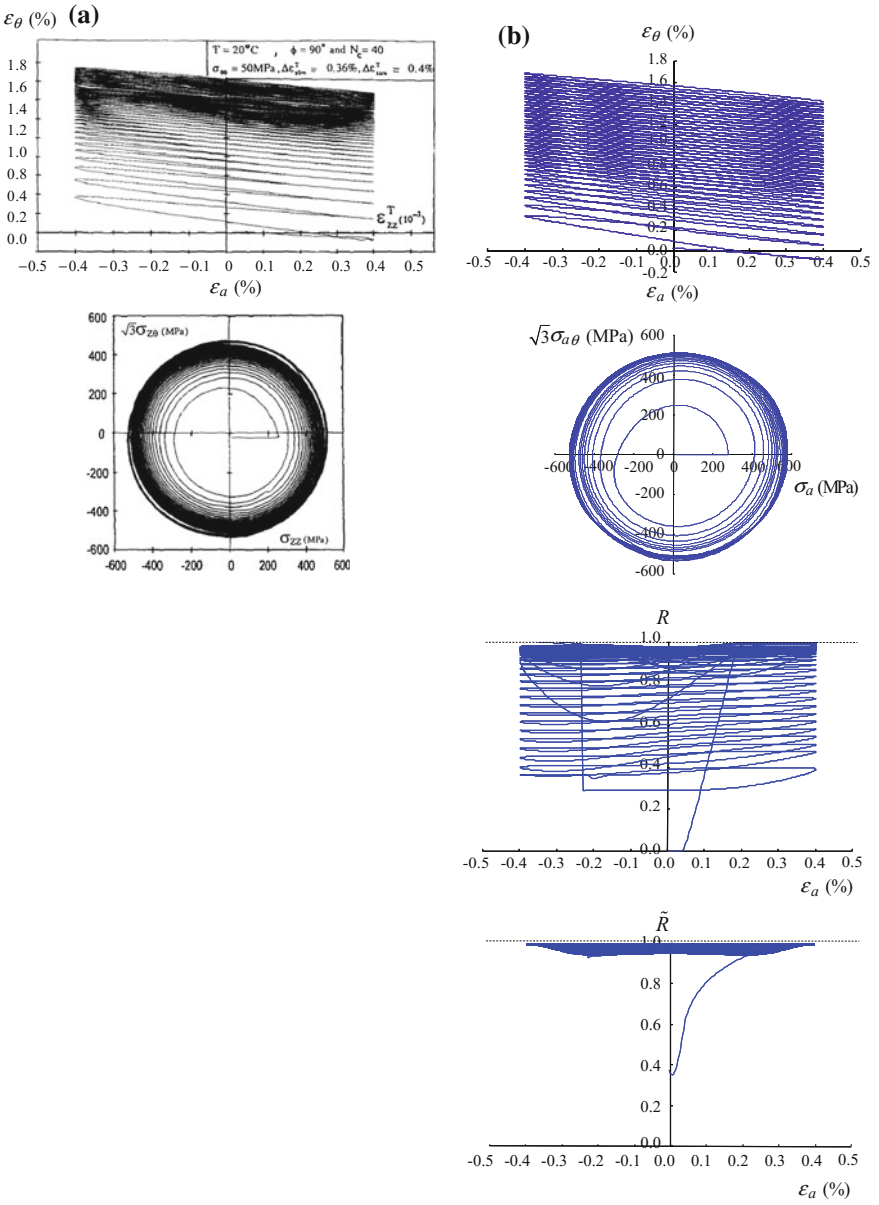

Fig. 10.9 Circular strain path loading given by the axial strain and the axial-circumferential engineering shear strain during 40 cycles after the uniaxial loading of austenitic 17–12 Mo SPH carbon stainless steel (Test data after Delobelle et al. 1995): **a** Test result, **b** Model simulation

The circular strain path in this test produces the spiral stress path approaching the circular stress path along the Mises yield surface which is expressed by the circle $\sqrt{\sigma_a^2 + (\sqrt{3}\sigma_{a\theta})^2} = F$ in the two-dimensional stress plane $(\sigma_a, \sqrt{3}\sigma_{a\theta})$. Here, note the following facts.

(1) The tangential-deviatoric stress rate is induced almost only in the component $((\boldsymbol{\sigma}'_t)_a, (\boldsymbol{\sigma}'_t)_{a\theta})$, and thus the tangential-inelastic strain rate is induced almost only in the component $((\mathbf{d}^t)_a, (\mathbf{d}^t)_{a\theta})$ in this test, if the isotropy is roughly assumed.
(2) The axial strain rate $(\mathbf{d})_a$ is composed of the axial elastoplastic strain rate $(\mathbf{d}^{ep})_a (=(\mathbf{d}^e)_a + (\mathbf{d}^p)_a)$ and the axial tangential-inelastic strain rate $(\mathbf{d}^t)_a$.
(3) The ratio of the axial component of tangential-inelastic strain rate, $(\mathbf{d}^t)_a$, to that of the elastoplastic strain rate, $(\mathbf{d}^{ep})_a$, is larger when the ratio $(\mathbf{d})_a/(\mathbf{d})_{a\theta}$ is larger in the strain space $(\varepsilon_a, \varepsilon_{a\theta})$. In other words, it is largest when the strain path passes through the top or the bottom of the circle in the strain space.
(4) The circumferential strain component ε_θ is almost independent of the tangential-inelastic strain rate.
(5) Then, the inclination of the $\varepsilon_\theta - \varepsilon_a$ curve, i.e. $\varepsilon_\theta/\varepsilon_a$ is smaller for the larger value of $\widetilde{c}$ in the strain plane $(\varepsilon_\theta, \varepsilon_a)$. Then, the strain path rises up higher compared with the test data in the strain plane $(\varepsilon_\theta, \varepsilon_a)$ if the tangential-strain rate is ignored by setting $\widetilde{c} = 0$ as shown in Fig. 10.10.

The importance of the introduction of the tangential-inelastic strain rate would have been definitely recognized by the verification shown above.

10.5 Springback and Residual Stress Analyses

The metal forming analyses are of importance in the industrial production. The analyses of the two typical phenomena, i.e. the springback analysis and the residual stress analysis by use of the subloading surface model will be described in this section.

(1) Springback analysis

The high tensile (strength) steel sheets and aluminum sheets exhibiting far larger springback than ordinary mild steel sheets are widely used in automobile industries. The springback cannot be described by the constitutive models which use the yield surface enclosing a purely-elastic domain, i.e. the conventional model and the cyclic kinematic hardening models (multi-surface, two-surface and superposed kinematic hardening models), since a plastic strain rate in the unloading process is not described appropriately by these models. Based on the two surface model, however, the method for the springback analysis was proposed by Yoshida and Uemori (2003) in which the Young's modulus is formulated to decrease but approach the saturated value with the equivalent plastic strain as shown in

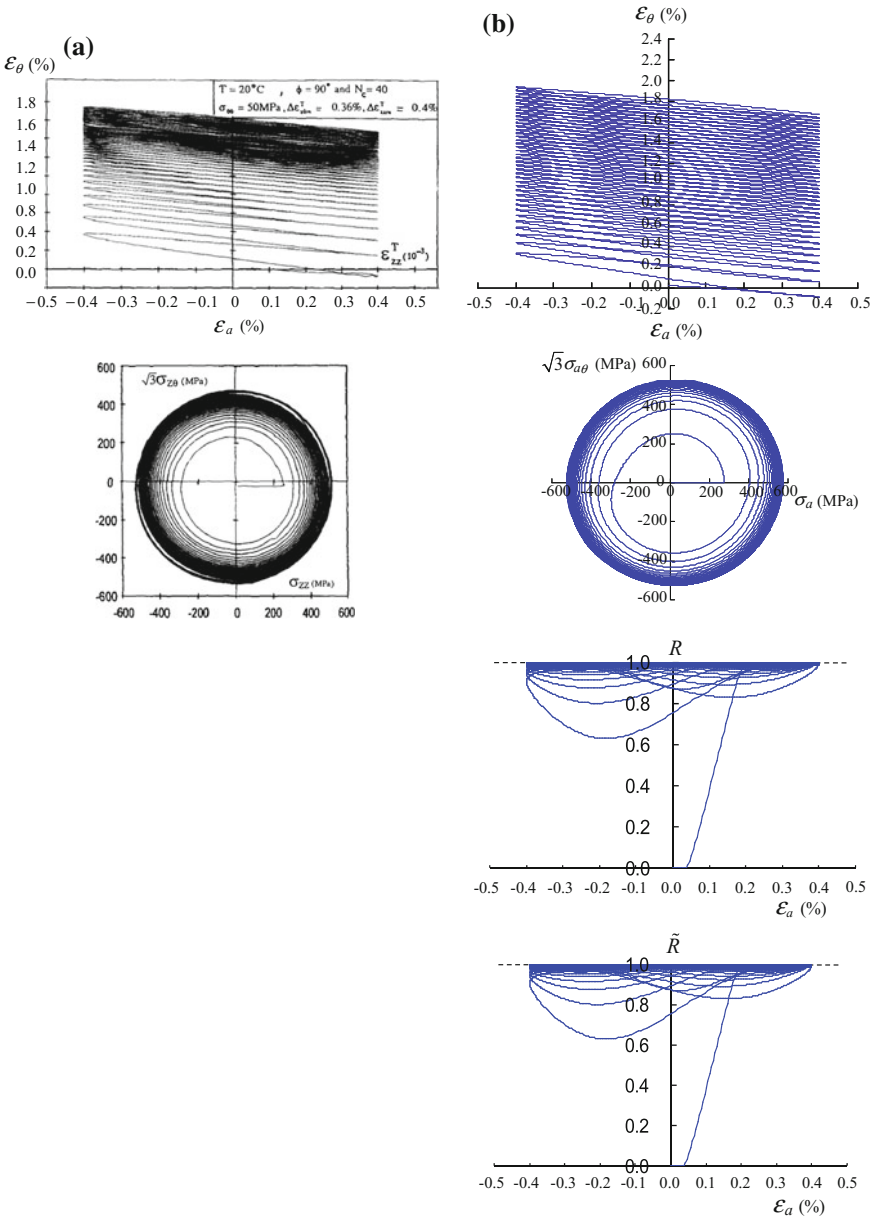

Fig. 10.10 Circular strain path loading given by the axial strain and the axial-circumferential engineering shear strain during 40 cycles after the uniaxial loading of austenitic 17–12 Mo SPH carbon stainless steel (Test data after Delobelle et al. 1995): **a** Test result, **b** Model simulation without tangential-inelasticity

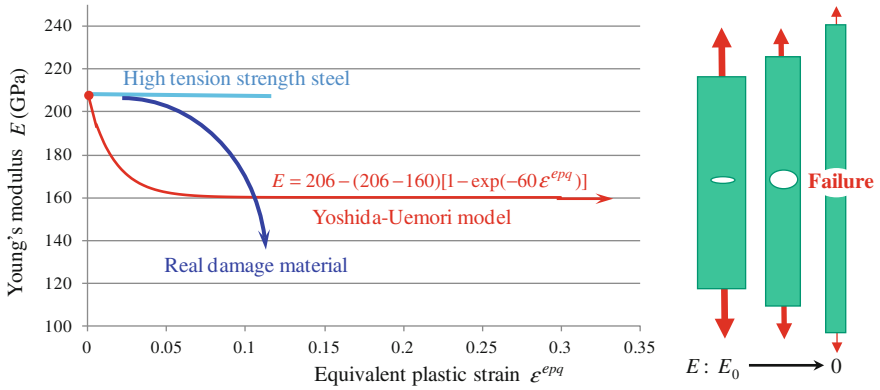

Fig. 10.11 Variation of Young's modulus with equivalent plastic strain: Physically-unacceptable prediction by Yoshida and Uemori (2003)

Fig. 10.11, which is calculated by the following equation for the *high tensile strength steel* (Yoshida and Uemori 2003).

$$E = E_0 - (E_0 - E_a)[1 - \exp(-\xi\varepsilon^{epq})] \text{ with } E_0 = 206,\ E_a = 160,\ \xi = 60$$

In fact, however, the purely elastic deformation is induced only at the initiation of stress reversal event and the plastic deformation induced in the unloading process to the stress free state would increase with the preceding plastic strain history. Nevertheless, the unloading process is regarded to be the purely elastic deformation process and then the Young's modulus is calculated from the inclination of straight line connecting the initial and the final points of the uniaxial unloading curve in the Yoshida and Uemori's model. Besides, the Young's moduli of real materials decreases acceleratingly to zero with the equivalent plastic strain in the continuing tension loading process if once it decreases as shown in Fig. 10.11. It is caused by the fact that the cracks grow increasingly so that not only the Young's modulus but also the hardening function F decreases in that loading process as has been revealed in the damage mechanics which will be described in Chapt. 14. Nevertheless, this fact based on the damage mechanics is also ignored and the so-called *prohibited technique* is used in the Yoshida and Uemori's model. Further, the incorporation of the *quasi-plastic-elastic strain* in the unloading process by Wagoner's group (cf. Sun and Wagoner 2011; Wagoner et al., 2013) is unacceptable physically in addition to causing the unnecessary complexity in formulation of constitutive relation. Besides, Barlat's group (cf. Lee et al., 2015) proposed the irrational friction model in which the friction coefficient is given by the multiplicative form consisting of the functions of sliding velocity and contact pressure, although the friction phenomenon is described rationally by the subloading-friction model which will be described in detail in Chapter 18. It is impertinent that the physically unacceptable model is adopted in the commercial softwares, i.e. the PAM-STAMP

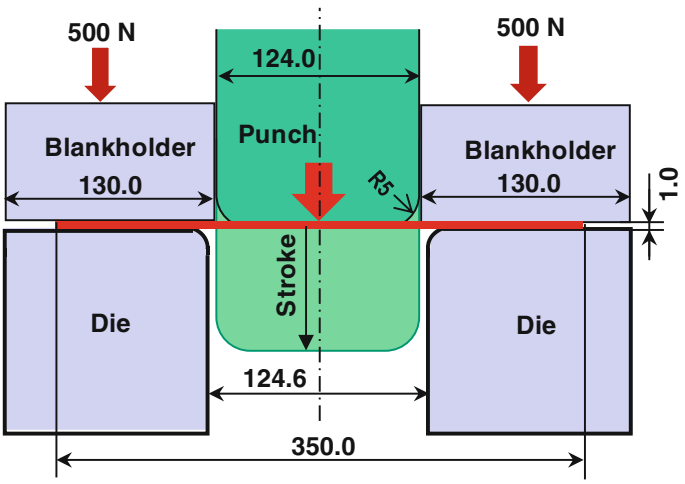

Fig. 10.12 Schematic illustration of the set-up of hat-bending after Yoshida and Uemori (2003)

and the LS-DYNA (Japan) and used widely in automobile industries. Constitutive equation capable of describing the plastic deformation in the unloading process should be incorporated for the springback analysis.

The pertinent calculation result of the springback is shown below, which was analyzed by Dr. Motoharu Tateishi (MSC Software, Ltd., Japan) by implementing the subloading surface model to the commercial software Marc (MSC Software, Ltd.).

The schematic illustration of the draw-bending (so-called *hat-bending*) is shown in Fig. 10.12, which was adopted by Yoshida and Uemori (2003).

The calculation results of the shapes of the sheet after the springback are shown in Fig. 10.13, choosing the die diameter 5 mm and using the following values of material parameters.

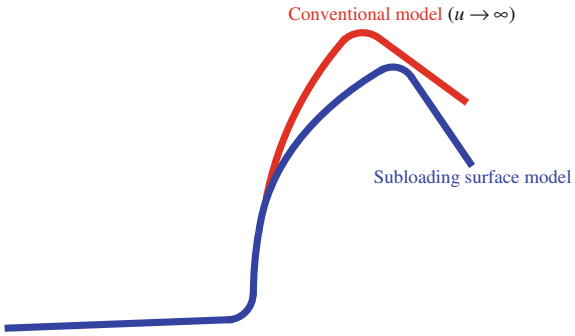

Fig. 10.13 Springback analysis

Material constants:

Elastic moduli: $E = 205,000\,\text{MPa},\ \nu = 0.3,$

Hardening $\begin{cases} \text{isotropic: } h_1 = 0.5,\ h_2 = 15, \\ \text{kinematic: } c_k = 3{,}000\ \text{MPa},\ \zeta = 0.5, \end{cases}$

Evolution of normal-yield ratio: $\bar{u} = 200, u_c = 3.5, R_e = 0.5, n = 1,$

Translation of elastic-core: $c = 3{,}000$ MPa, $\xi = 0.7,$

Stagnation of isotropic hardening: $C = 0.5, \varsigma = 20, \upsilon = 1,$

Initial values:

Isotropic hardening function: $F_0 = 400\,\text{MPa}.$

The enough springback is predicted, which is caused by the plastic deformation in the stress-releasing process by virtue of the advantage of the subloading surface model describing the plastic strain rate due to the rate of stress inside the yield surface. In contrast, the spingback is predicted just slightly by the conventional elastoplastic model which is realized by using the large value for the material constant in the evolution of the normal-yield ratio $\overline{u} = 100,000$ only in the springback process. Then, the importance is recognized for the introduction of the rigorous elastoplastic model, i.e. the subloading surface model capable of describing the plastic strain rate in the stress-reducing process appropriately. Hereinafter, it is desirable that the prediction of springback behavior will be executed by the pertinent analysis exploiting the subloading surface model, aiming at the epochal improvement of the prediction of the springback behavior in industries.

(1) **Residual stress analysis** (Higuchi and Okamura 2016)

The prediction of the residual stress is of importance in the metal forming process. The estimations of residual stress change due to cyclic loading by the conventional elastoplasticity model and the subloading surface model are shown below, which was examined by Higuchi and Okamura (2016).

A four-point cyclic bending test was conducted to examine the change of the residual stress in the cyclic loading process. A specimen with a width of 13 mm, a thickness of 13 mm and a length of 100 mm was cut from a seamless steel pipe P110. The specimen was loaded under a four-point bend configuration with the intervals of 20 mm between the inner rollers and 80 mm between the outer rollers as shown in Fig. 10.14. At first, the specimen was plastically deformed by static bending load corresponding to the maximum bending stress of 900 MPa. After the unloading of the static bending load, the compressive residual stress was generated in the side of outer rollers and the tensile residual stress in the side of inner rollers. The distribution of the residual stress was measured by the X-ray stress measurement method. Then, the specimen was turned upside down, so that the side of outer rollers was in the tensile residual stress state. Sinusoidal waveform load between 5 and 100 % of 900 MPa was applied 20 times to the specimen. The maximum

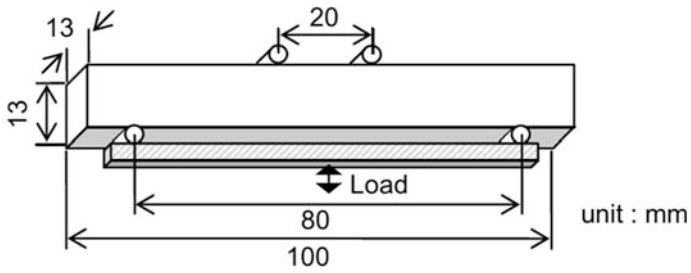

Fig. 10.14 Configuration of the four-point bending test

bending stress was 500 MPa. The distributions of the residual stress after cyclic loading were measured by the X-ray stress measurement method.

The simulations by the Chaboche model described in Sect. 8.2.5 and the subloading surface model described in this chapter are executed, while the commercial software Abaqus is used in the simulation by the Chaboche model. First, material constants of these two models were determined so as to fit to the test data of uniaxial cyclic loading of a round bar specimen of P110 as shown in Fig. 10.15. The test data can be simulated accurately by the subloading surface model. On the other hand, the simulation by the Chaboche model is not in agreement with the test data. Especially, it was difficult to simulate appropriately the smooth elastic-plastic transition in the reverse loading processes by the Chaboche model.

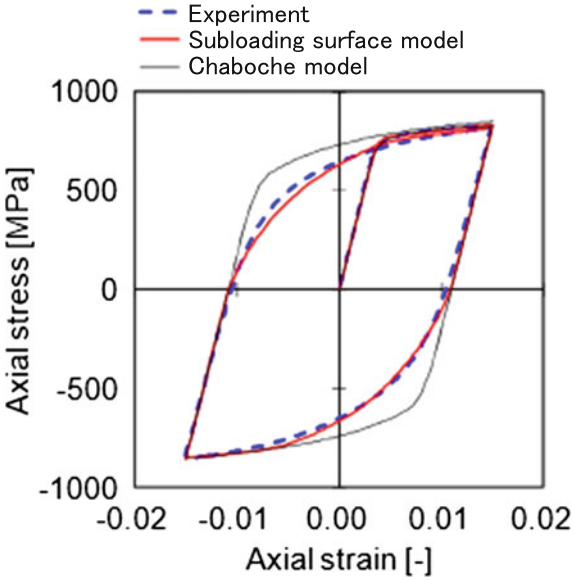

Fig. 10.15 Comparison of stress-strain curves between experiment and simulations in uniaxial loading

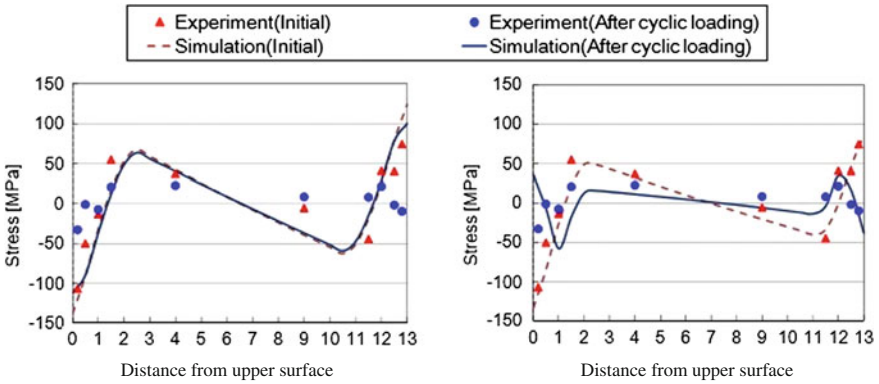

(a) Chaboche model (b) Subloading surface model

Fig. 10.16 Comparison of distributions of residual stresses before and after cyclic loading between experiment and simulations

Measured distributions of the residual stresses after the initial loading and the 20 times cyclic loading are simulated by the two models as shown in Fig. 10.16. The horizontal axis denotes the distance from upper surface to lower surface at center of the specimen. The initial residual stress distributions are simulated well by both of these models. As for the residual stress distribution after cyclic loading, however, the decreases of the residual stresses near the upper and the lower surfaces of the specimen is accurately simulated by the subloading surface model, whereas they are not simulated by the Chaboche model. This would be caused by the fact that the subloading surface model is capable of describing the cyclic loading behavior more accurately than the other constitutive models.

10.6 Orthotropic Anisotropy

The kinematic hardening incorporated in the foregoing is regarded to be the induced anisotropy. On the other hand, various inherent anisotropies are induced in the manufacturing process of metals. The typical inherent anisotropy is the *orthotropic anisotropy* formulated by Hill (1948).

Now, consider the general yield function in the quadratic form shown as follows:

$$f(\sigma_{ij}) = \sqrt{\frac{1}{2} C_{ijkl} \sigma_{ij} \sigma_{kl}} \tag{10.33}$$

where C_{ijkl} is the fourth-order anisotropic tensor having eighty-one components fulfilling the symmetry

$$C_{ijkl} = C_{ijlk} = C_{jikl} = C_{jilk} = C_{klij} = C_{klji} = C_{lkij} = C_{lkji} \tag{10.34}$$

by the minor symmetries $C_{ijkl} = C_{ijlk} = C_{jikl}$ based on the symmetry of the stress tensor $\sigma_{ij} = \sigma_{ji}$ and the major symmetries $C_{ijkl} = C_{klij}$ based on $C_{ijkl}\sigma_{ij}\sigma_{kl} = C_{klij}\sigma_{kl}\sigma_{ij} = C_{klij}\sigma_{ij}\sigma_{kl}$. Then, the independent components is reduced to twenty-one leading to

$$\begin{aligned}
&C_{ijkl}\sigma_{ij}\sigma_{kl} \\
&= C_{1111}\sigma_{11}^2 + 2C_{1122}\sigma_{11}\sigma_{22} + 2C_{1133}\sigma_{11}\sigma_{33} + 2C_{1112}\sigma_{11}\sigma_{12} + 2C_{1123}\sigma_{11}\sigma_{23} + 2C_{1131}\sigma_{11}\sigma_{33} \\
&\quad + C_{2222}\sigma_{22}^2 + 2C_{2233}\sigma_{22}\sigma_{33} + 2C_{2212}\sigma_{22}\sigma_{12} + 2C_{2223}\sigma_{22}\sigma_{23} + 2C_{2231}\sigma_{22}\sigma_{31} \\
&\quad + C_{3333}\sigma_{33}^2 + 2C_{3312}\sigma_{33}\sigma_{12} + 2C_{3323}\sigma_{33}\sigma_{23} + 2C_{3331}\sigma_{33}\sigma_{31} \\
&\quad + C_{1212}\sigma_{12}^2 + 2C_{1223}\sigma_{12}\sigma_{23} + 2C_{1231}\sigma_{12}\sigma_{31} \\
&\quad + C_{2323}\sigma_{23}^2 + 2C_{2331}\sigma_{23}\sigma_{31} \\
&\quad + C_{3131}\sigma_{31}^2
\end{aligned} \tag{10.35}$$

which is the general form of yield function in the quadratic form.

Here, assuming the plastic incompressibility, it holds that

$$\begin{aligned}
(\partial(2f^2)/\partial\sigma_{pq})\delta_{pq} &= (\partial C_{ijkl}\sigma_{ij}\sigma_{kl}/\partial\sigma_{pq})\delta_{pq} \\
&= C_{ijkl}\delta_{pi}\delta_{qj}\sigma_{kl}\delta_{pq} + C_{ijkl}\sigma_{ij}\delta_{pk}\delta_{ql}\delta_{pq} \\
&= C_{ppkl}\sigma_{kl} + C_{ijpp}\sigma_{ij} = C_{ppkl}\sigma_{kl} + C_{ppij}\sigma_{ij} \\
&= 2C_{ppkl}\sigma_{kl} = 0
\end{aligned}$$

This relation must hold for any σ_{ij} and thus one obtains

$$C_{ppkl} = C_{ijqq} = 0 \tag{10.36}$$

which leads to

$$\left.\begin{aligned} C_{1111} + C_{1122} + C_{1133} &= 0 \\ C_{2211} + C_{2222} + C_{2233} &= 0 \\ C_{3311} + C_{3322} + C_{3333} &= 0 \end{aligned}\right\} \tag{10.37}$$

$$\left.\begin{aligned} C_{1112} + C_{2212} + C_{3312} &= 0 \\ C_{1123} + C_{2223} + C_{3323} &= 0 \\ C_{1131} + C_{2231} + C_{3331} &= 0 \end{aligned}\right\} \rightarrow \left.\begin{aligned} C_{3312} &= -(C_{1112} + C_{2212}) \\ C_{1123} &= -(C_{2223} + C_{3323}) \\ C_{2231} &= -(C_{1131} + C_{3331}) \end{aligned}\right\} \tag{10.38}$$

The substitution of Eq. (10.38) into Eq. (10.35) gives the expression

$$
\begin{aligned}
&C_{ijkl}\sigma_{ij}\sigma_{kl}\\
&= C_{1111}\sigma_{11}^2 + 2C_{1122}\sigma_{11}\sigma_{22} + 2C_{1133}\sigma_{11}\sigma_{33} + 2C_{1112}\sigma_{11}\sigma_{12} - 2(C_{2223}\\
&\quad + C_{3323})\sigma_{11}\sigma_{23} + 2C_{1131}\sigma_{11}\sigma_{31}\\
&\quad + C_{2222}\sigma_{22}^2 + 2C_{2233}\sigma_{22}\sigma_{33} + 2C_{2212}\sigma_{22}\sigma_{12} + 2C_{2223}\sigma_{22}\sigma_{23} - 2(C_{1131} + C_{3331})\sigma_{22}\sigma_{33}\\
&\quad + C_{3333}\sigma_{33}^2 - 2(C_{1112} + C_{2212})\sigma_{33}\sigma_{12} + 2C_{3323}\sigma_{33}\sigma_{23} + 2C_{3331}\sigma_{33}\sigma_{31}\\
&\quad + C_{1212}\sigma_{12}^2 + 2C_{1223}\sigma_{123}\sigma_{23} + 2C_{1231}\sigma_{12}\sigma_{31}\\
&\quad + C_{2323}\sigma_{23}^2 + 2C_{2331}\sigma_{23}\sigma_{31}\\
&\quad + C_{3131}\sigma_{31}^2
\end{aligned}
\tag{10.39}
$$

Further, noting Eq. (10.37), the terms in the form $C_{iijj}\sigma_{ii}\sigma_{jj}$ (no sum) are written as

$$
\begin{aligned}
&C_{1111}\sigma_{11}^2 + C_{2222}\sigma_{22}^2 + C_{3333}\sigma_{33}^2 + 2C_{1122}\sigma_{11}\sigma_{22} + 2C_{2233}\sigma_{22}\sigma_{33} + 2C_{1133}\sigma_{11}\sigma_{33}\\
&\quad = C_{1111}\sigma_{11}^2 + C_{2222}\sigma_{22}^2 + C_{3333}\sigma_{33}^2\\
&\qquad -C_{1122}(\sigma_{11}-\sigma_{22})^2 + C_{1122}\sigma_{11}^2 + C_{1122}\sigma_{22}^2\\
&\qquad -C_{2233}(\sigma_{22}-\sigma_{33})^2 + C_{2233}\sigma_{22}^2 + C_{2233}\sigma_{33}^2\\
&\qquad -C_{1133}(\sigma_{33}-\sigma_{11})^2 + C_{1133}\sigma_{33}^2 + C_{2233}\sigma_{11}^2\\
&\quad = (C_{1111} + C_{1122} + C_{2233})\sigma_{11}^2 + (C_{1122} + C_{2222} + C_{2233})\sigma_{22}^2\\
&\qquad + (C_{1133} + C_{2233} + C_{3333})\sigma_{33}^2\\
&\qquad -C_{1122}(\sigma_{11}-\sigma_{22})^2 - C_{2233}(\sigma_{22}-\sigma_{33})^2 - C_{1133}(\sigma_{33}-\sigma_{11})^2\\
&\quad = -C_{1122}(\sigma_{11}-\sigma_{22})^2 - C_{2233}(\sigma_{22}-\sigma_{33})^2 - C_{1133}(\sigma_{33}-\sigma_{11})^2
\end{aligned}
\tag{10.40}
$$

Then, by setting

$$
\left.
\begin{aligned}
&a_1 \equiv -C_{1122}, a_2 \equiv -C_{2233}\, a_3 \equiv -C_{1133}\\
&a_4 \equiv -2C_{1112}, a_5 \equiv -2C_{2212}, a_6 \equiv -C_{2223}\\
&a_7 \equiv -2C_{3323}\, a_8 \equiv -2C_{3331}, a_9 \equiv -2C_{1131}\\
&a_{10} \equiv 2C_{1223}, a_{11} \equiv 2C_{2331}\, a_{12} \equiv 2C_{1231}\\
&a_{13} \equiv C_{1212}, a_{14} \equiv C_{2323}\, a_{15} \equiv C_{3131}
\end{aligned}
\right\}
\tag{10.41}
$$

and substituting Eqs. (10.39) and (10.40) with Eq. (10.41) into Eq. (10.39) reads:

$$
\begin{aligned}
C_{ijkl}\sigma_{ij}\sigma_{kl} &= a_1(\sigma_{11}-\sigma_{22})^2 + a_2(\sigma_{22}-\sigma_{33})^2 + a_3(\sigma_{33}-\sigma_{11})^2\\
&\quad + \{a_4(\sigma_{33}-\sigma_{11}) + a_5(\sigma_{33}-\sigma_{22})\}\sigma_{12}\\
&\quad + \{a_6(\sigma_{11}-\sigma_{22}) + a_7(\sigma_{22}-\sigma_{33})\}\sigma_{23}\\
&\quad + \{a_8(\sigma_{22}-\sigma_{33}) + a_9(\sigma_{22}-\sigma_{11})\}\sigma_{31}\\
&\quad + a_{10}\sigma_{12}\sigma_{23} + a_{11}\sigma_{23}\sigma_{31} + a_{12}\sigma_{31}\sigma_{12}\\
&\quad + a_{13}\sigma_{12}^2 + a_{14}\sigma_{23}^2 + a_{15}\sigma_{31}^2
\end{aligned}
\tag{10.42}
$$

Equation (10.42) is the general yield function for the plastically-incompressible materials in the quadratic form.

Now, assume orthotropic anisotropy. Then, if we describe the yield surface by the coordinate axes selected to the principal axes $\{\widehat{\mathbf{e}}_i\}$ of orthotropic anisotropy, the yield function is independent of the sign of shear stress components in this coordinate system. Therefore, it must hold that

$$a_4 = a_5 = a_6 = a_7 = a_8 = a_9 = a_{10} = a_{11} = a_{12} = 0$$

Here, replacing the symbols a_i as

$$F = a_1, G = a_2, H = a_3, L = a_{13}/2, M = a_{14}/2, H = a_{15}/2$$

used by Hill (1948), Eq. (10.42) leads to the Hill's yield condition with orthotropic anisotropy:

$$\boxed{\frac{1}{2}\sqrt{F(\sigma_{11}-\sigma_{22})^2 + G(\sigma_{22}-\sigma_{33})^2 + H(\sigma_{33}-\sigma_{11})^2 + 6(L\sigma_{12}^2 + M\sigma_{23}^2 + N\sigma_{31}^2)} = F(H)} \tag{10.43}$$

Here, note that for the isotropic material all the material parameters are unity, i.e. $F = G = H = L = M = N = 1$ holds and thus Eq. (10.43) is reduced to $\sqrt{3/2}\|\hat{\boldsymbol{\sigma}}'\| = F(H)$ which is the equivalent stress, noting Eq. (1.187). While Eq. (10.43) is the expression on the principal axis $\{\widehat{\mathbf{e}}_i\}$ of orthotropic anisotropy, it is rewritten by the following equation stipulating this fact.

$$\frac{1}{2}\sqrt{F(\widehat{\sigma}_{11}-\widehat{\sigma}_{22})^2 + G(\widehat{\sigma}_{22}-\widehat{\sigma}_{33})^2 + H(\widehat{\sigma}_{33}-\widehat{\sigma}_{11})^2 + 6(L\widehat{\sigma}_{12}^2 + M\widehat{\sigma}_{23}^2 + N\widehat{\sigma}_{31}^2)} = F(H) \tag{10.44}$$

or

$$\bar{F}(\widehat{\sigma}_{11}-\widehat{\sigma}_{22})^2 + \bar{G}(\widehat{\sigma}_{22}-\widehat{\sigma}_{33})^2 + \bar{H}(\widehat{\sigma}_{33}-\widehat{\sigma}_{11})^2 + 6(\bar{L}\widehat{\sigma}_{12}^2 + \bar{M}\widehat{\sigma}_{23}^2 + \bar{N}\widehat{\sigma}_{31}^2) = 1 \tag{10.45}$$

where

$$\left.\begin{aligned} \bar{H} &\equiv \frac{H}{[2F(H)]^2}, \bar{G} \equiv \frac{G}{[2F(H)]^2}, \overline{F} \equiv \frac{F}{[2F(H)]^2} \\ \bar{L} &\equiv \frac{L}{[2F(H)]^2}, \bar{M} \equiv \frac{L}{[2F(H)]^2}, \bar{N} \equiv \frac{L}{[2F(H)]^2} \end{aligned}\right\} \tag{10.46}$$

Denoting $\widehat{\sigma}_{11}, \widehat{\sigma}_{22}, \widehat{\sigma}_{33}, \widehat{\sigma}_{12}, \widehat{\sigma}_{23}$ and $\widehat{\sigma}_{31}$ by the yield stress by $\widehat{\sigma}^{y}_{1}, \widehat{\sigma}^{y}_{2}, \widehat{\sigma}^{y}_{3}$, $\widehat{\sigma}^{y}_{12}, \widehat{\sigma}^{y}_{23}$ and $\widehat{\sigma}^{y}_{31}$, respectively, when only each stress applies, one has

$$\left.\begin{array}{l}(\bar{H}+\bar{F})\widehat{\sigma}^{y2}_{1}=1,(\bar{G}+\bar{F})\widehat{\sigma}^{y2}_{2}=1,(\bar{G}+\bar{H})\widehat{\sigma}^{y2}_{3}=1\\ 6\bar{L}\widehat{\tau}^{y2}_{12}=1,6\bar{M}\widehat{\tau}^{y2}_{23}=1,6\bar{N}\widehat{\tau}^{y2}_{31}=1\end{array}\right\} \tag{10.47}$$

from which the material parameters are given by

$$\left.\begin{array}{l}\bar{F}=\dfrac{1}{2}\left(\dfrac{1}{\widehat{\sigma}^{y2}_{1}}+\dfrac{1}{\widehat{\sigma}^{y2}_{2}}+\dfrac{1}{\widehat{\sigma}^{y2}_{3}}\right)\\ \bar{G}=\dfrac{1}{2}\left(\dfrac{1}{\widehat{\sigma}^{y2}_{2}}+\dfrac{1}{\widehat{\sigma}^{y2}_{3}}+\dfrac{1}{\widehat{\sigma}^{y2}_{1}}\right)\\ \bar{H}=\dfrac{1}{2}\left(\dfrac{1}{\widehat{\sigma}^{y2}_{3}}+\dfrac{1}{\widehat{\sigma}^{y2}_{1}}+\dfrac{1}{\widehat{\sigma}^{y2}_{2}}\right)\\ \bar{L}=\dfrac{1}{6\widehat{\tau}^{y2}_{12}},\ \bar{M}=\dfrac{1}{6\widehat{\tau}^{y2}_{23}},\ \bar{N}=\dfrac{1}{6\widehat{\tau}^{y2}_{23}}\end{array}\right\} \tag{10.48}$$

Equation (10.44) is reduced under the uniaxial loading in the sheet metal forming as follows:

$$\frac{1}{2}\sqrt{(F+H)}\widehat{\sigma}_{11}=F(H)\quad\text{or}\quad(\bar{F}+\bar{H})\widehat{\sigma}^{2}_{11}=F(H) \tag{10.49}$$

Further, under the plane stress condition observed in the sheet metal forming it holds that $\widehat{\sigma}_{23}=\widehat{\sigma}_{31}=\widehat{\sigma}_{33}=0$ and thus Eqs. (10.44) and (10.45) are reduced to

$$\frac{1}{2}\sqrt{(F+H)\widehat{\sigma}^{2}_{11}-2F\widehat{\sigma}_{11}\widehat{\sigma}_{22}+(F+G)\widehat{\sigma}^{2}_{22}+6L\widehat{\sigma}^{2}_{12}}=F(H) \tag{10.50}$$

i.e.

$$(\bar{F}+\bar{H})\widehat{\sigma}^{2}_{11}-2\bar{F}\widehat{\sigma}_{11}\widehat{\sigma}_{22}+(\bar{F}+\bar{G})\widehat{\sigma}^{2}_{22}+6\bar{L}\widehat{\sigma}^{2}_{12}=1 \tag{10.51}$$

Equation (10.51) is described in the state that the principal stress directions coincide with the orthogonal anisotropy axes as follows:

$$(\bar{F}+\bar{H})\widehat{\sigma}^{2}_{1}-2\bar{F}\widehat{\sigma}_{1}\widehat{\sigma}_{2}+(\bar{F}+\bar{G})\widehat{\sigma}^{2}_{2}=1 \tag{10.52}$$

The plastic strain rate is given for as follows:

$$\left.\begin{array}{l}d^{p}_{1}/\dot{\lambda}=2(\bar{F}+\bar{H})\widehat{\sigma}_{1}-2\bar{F}\widehat{\sigma}_{2}\\ d^{p}_{2}/\dot{\lambda}=-2\bar{F}\widehat{\sigma}_{1}+2(\bar{F}+\bar{G})\widehat{\sigma}_{2}\\ d^{p}_{3}/\dot{\lambda}=-2\bar{H}\widehat{\sigma}_{1}-2\bar{G}\widehat{\sigma}_{2}\end{array}\right\} \tag{10.53}$$

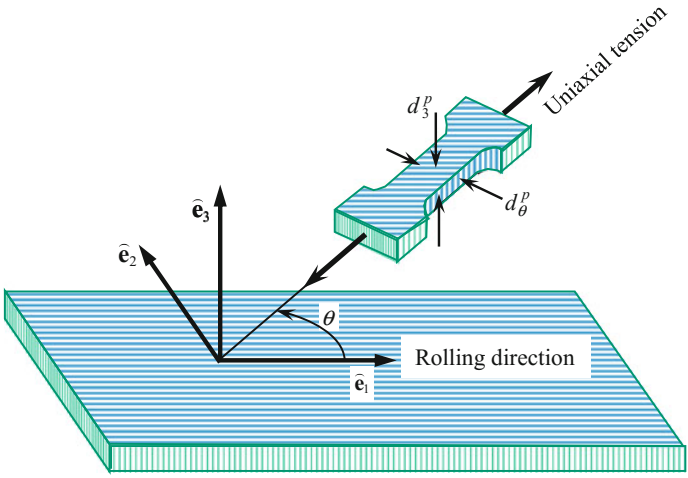

Fig. 10.17 Uniaxial tension test for *R*-value for metal formed by rolling process

The orthogonal anisotropy is induced seriously in the rolling process for the sheet metal forming. Choosing the axes $\widehat{\mathbf{e}}_1, \widehat{\mathbf{e}}_2, \widehat{\mathbf{e}}_3$ to the rolling, the traverse, and the thickness directions, respectively, the following *R*-value is adopted widely in order to evaluate the intensity of the orthotropy.

$$R_\theta = \frac{d_\theta^p}{d_3^p} \tag{10.54}$$

where $d_\theta^p(<0)$ is the lateral strain rate measured from the uniaxial tension test of the test specimen cut out at the angle θ measured counterclockwise from the rolling direction. The plastic strain rate $d_3^p(<0)$ in the thickness direction is calculated from the axial and the lateral strain rates by the assumption of plastic incompressibility (see Fig. 10.17). $R = 1$ means the isotropy. A small *R*-value means that the produced sheet metal is easily thinned resulting in an easy failure. It follows from Eq. (10.53) that

$$\left.\begin{aligned} R_0 &= \frac{d_2^p}{d_3^p} = \frac{\bar{F}}{\bar{H}} \quad \text{for } \widehat{\sigma}_2 = \widehat{\sigma}_3 = 0 \\ R_{90} &= \frac{d_1^p}{d_3^p} = \frac{\bar{F}}{\bar{G}} \quad \text{for } \widehat{\sigma}_1 = \widehat{\sigma}_3 = 0 \end{aligned}\right\} \tag{10.55}$$

Substituting $\bar{F} = R_0\bar{H}$ due to Eq. (10.55) into Eq. (10.52), one has

$$(\bar{H} + R_0\bar{H})\widehat{\sigma}_1^2 + (\bar{G} + R_0\bar{H})\widehat{\sigma}_2^2 - 2R_0\bar{H}\widehat{\sigma}_1\widehat{\sigma}_2 = 1$$

leading to

$$\widehat{\sigma}_1^2 + \frac{\bar{G} + R_0\bar{H}}{(1+R_0)\bar{H}}\widehat{\sigma}_2^2 - \frac{2R_0}{1+R_0}\widehat{\sigma}_1\widehat{\sigma}_2 = \frac{1}{(1+R_0)\bar{H}} \tag{10.56}$$

Substituting Eq. (10.48) into Eq. (10.55), it follows that

$$\left.\begin{aligned}(1+R_0)\frac{1}{\widehat{\sigma}_3^{y2}} - (1+R_0)\frac{1}{\widehat{\sigma}_2^{y2}} &= (1-R_0)\frac{1}{\widehat{\sigma}_1^{y2}}\\ (1+R_{90})\frac{1}{\widehat{\sigma}_3^{y2}} - (1-R_{90})\frac{1}{\widehat{\sigma}_2^{y2}} &= (1+R_{90})\frac{1}{\widehat{\sigma}_1^{y2}}\end{aligned}\right\}$$

By solving this equation, one has

$$\left.\begin{aligned}\frac{1}{\widehat{\sigma}_2^{y2}} &= \frac{R_0(1+R_{90})}{(1+R_0)R_{90}}\frac{1}{\widehat{\sigma}_1^{y2}}\\ \frac{1}{\widehat{\sigma}_3^{y2}} &= \frac{R_0+R_{90}}{(1+R_0)R_{90}}\frac{1}{\widehat{\sigma}_1^{y2}}\end{aligned}\right\} \tag{10.57}$$

Substituting Eq. (10.57) into Eq. (10.48), it follows that

$$\left.\begin{aligned}\bar{G} &= \frac{R_0}{(1+R_0)R_{90}}\frac{1}{\widehat{\sigma}_1^{y2}}\\ \bar{H} &= \frac{1}{1+R_0}\frac{1}{\widehat{\sigma}_1^{y2}}\end{aligned}\right\} \tag{10.58}$$

from which we have

$$\left.\begin{aligned}\frac{\bar{G} + R_0\bar{H}}{(1+R_0)\bar{H}} &= \frac{R_0(1+R_{90})}{(1+R_0)R_{90}}\\ \frac{1}{(1+R_0)\bar{H}} &= \widehat{\sigma}_1^{y2}\end{aligned}\right\} \tag{10.59}$$

Substituting Eq. (10.59) into Eq. (10.56), it follows that

$$\boxed{\widehat{\sigma}_1^2 + \frac{R_0(1+R_{90})}{(1+R_0)R_{90}}\widehat{\sigma}_2^2 - \frac{2R_0}{1+R_0}\widehat{\sigma}_1\widehat{\sigma}_2 = \widehat{\sigma}_1^{y_2}} \tag{10.60}$$

Equation (10.51) is rewritten as

$$\left[\frac{1}{4}(\bar{G}+\bar{H})+\frac{1}{4}(\bar{G}+\bar{H}+4\bar{F})-\frac{1}{2}(\bar{G}-\bar{H})\right]\widehat{\sigma}_{11}^2+\left[\frac{2}{4}(\bar{G}+\bar{H})-\frac{2}{4}(\bar{G}+\bar{H}+4\bar{F})\right]\widehat{\sigma}_{11}\widehat{\sigma}_{22}$$
$$+\left[\frac{1}{4}(\bar{G}+\bar{H})+\frac{1}{4}(\bar{G}+\bar{H}+4\bar{F})+\frac{1}{2}(\bar{G}-\bar{H})\right]\widehat{\sigma}_{22}^2+6\bar{L}\widehat{\sigma}_{12}^2=1$$

which is arranged as follows:

$$\frac{1}{4}(\bar{G}+\bar{H})(\widehat{\sigma}_{11}+\widehat{\sigma}_{22})^2+\frac{1}{4}(\bar{G}+\bar{H}+4\bar{F})(\widehat{\sigma}_{11}-\widehat{\sigma}_{22})^2$$
$$-\frac{1}{2}(\bar{G}-\bar{H})(\widehat{\sigma}_{11}^2-\widehat{\sigma}_{22}^2)+6\bar{L}\widehat{\sigma}_{12}^2=1 \tag{10.61}$$

Denoting the angle measured in the counterclockwise direction from the principal axes of anisotropy to the principal stress as α and substituting the relations

$$\widehat{\sigma}_{11}+\widehat{\sigma}_{22}=\sigma_1+\sigma_2,\ \widehat{\sigma}_{11}-\widehat{\sigma}_{22}=(\sigma_1-\sigma_2)\cos 2\alpha,\ 2\widehat{\sigma}_{12}=(\sigma_1-\sigma_2)\sin 2\alpha \tag{10.62}$$

into Eq. (10.61), one has

$$\frac{1}{4}(\bar{G}+\bar{H})(\sigma_1+\sigma_2)^2+\frac{1}{4}(\bar{G}+\bar{H}+4\bar{F})(\sigma_1-\sigma_2)^2\cos^2 2\alpha$$
$$-\frac{1}{2}(\bar{G}-\bar{H})(\sigma_1^2-\sigma_2^2)\cos 2\alpha+\frac{3}{2}\bar{L}(\sigma_1-\sigma_2)^2\sin^2 2\alpha=1$$

which is rewritten as

$$(\sigma_1+\sigma_2)^2-2a(\sigma_1^2-\sigma_2^2)\cos 2\alpha+b(\sigma_1-\sigma_2)^2\cos^2 2\alpha$$
$$+6\frac{\bar{L}}{\bar{G}+\bar{H}}(\sigma_1-\sigma_2)^2=\frac{4}{\bar{G}+\bar{H}} \tag{10.63}$$

where

$$a\equiv\frac{\bar{G}-\bar{H}}{\bar{G}+\bar{H}},b\equiv\frac{\bar{G}+\bar{H}+4\bar{F}-6\bar{L}}{\bar{G}+\bar{H}} \tag{10.64}$$

Here, denoting the yielding strength in the equi-two axis tension as σ and that of the pure shear as τ, it follows from Eq. (10.51) that

$$\sigma\equiv(\bar{H}+\bar{G})^{-1/2},\ \tau\equiv(6\bar{L})^{-1/2} \tag{10.65}$$

The substitution of Eq. (10.65) into Eq. (10.63) leads to

$$(\sigma_1+\sigma_2)^2+\left(\frac{\sigma}{\tau}\right)^2(\sigma_1-\sigma_2)^2-2a(\sigma_1^2-\sigma_2^2)\cos 2\alpha+b(\sigma_1$$
$$-\sigma_2)^2\cos^2 2\alpha=(2\sigma)^2 \tag{10.66}$$

Equation (10.66) is extended to the following equation for the in-plane isotropy with the material constant $m(\geq 1)$.

$$|\sigma_1+\sigma_2|^m+\left(\frac{\sigma}{\tau}\right)^m|\sigma_1-\sigma_2|^m=(2\sigma)^m \tag{10.67}$$

Hill (1990) proposed the following extended orthotropic yield condition from Eqs. (10.66) and (10.67).

$$\begin{aligned}&|\sigma_1+\sigma_2|^m+\left(\frac{\sigma}{\tau}\right)^m|\sigma_1-\sigma_2|^m\\&\quad+|\sigma_1^2+\sigma_2^2|^{(m/2)-1}[-2a(\sigma_1^2-\sigma_2^2)+b(\sigma_1-\sigma_2)^2\cos 2\alpha]\cos 2\alpha=(2\sigma)^m\end{aligned} \tag{10.68}$$

Equation (10.68) includes the five material constants, i.e. the yield stress σ,τ and the dimensionless number a,b,m. It is reduced to Eq. (10.66) for $m=2$ and to Eq. (10.67) for $a=b=0$ (or $\alpha=\pi/4$). By use of Eq. (10.62), Eq. (10.68) is rewritten in the anisotropic axes as follows:

$$\begin{aligned}&|\widehat{\sigma}_{11}+\widehat{\sigma}_{22}|^m+\left(\frac{\sigma}{\tau}\right)^m\left|(\widehat{\sigma}_{11}-\widehat{\sigma}_{22})^2+4\widehat{\sigma}_{12}^2\right|^{m/2}\\&\quad+\left|(\widehat{\sigma}_{11}+\widehat{\sigma}_{22})^2+4\widehat{\sigma}_{12}^2\right|^{(m/2)-1}[-2a(\widehat{\sigma}_{11}^2-\widehat{\sigma}_{22}^2)+b(\widehat{\sigma}_{11}-\widehat{\sigma}_{22})^2]=(2\sigma)^m\end{aligned} \tag{10.69}$$

Generally, the yield surface is described in the principal axes of anisotropy as follows:

$$f(\widehat{\sigma}_{ij})=F(H) \tag{10.70}$$

where

$$\widehat{\boldsymbol{\sigma}}=\widehat{\mathbf{R}}^T\boldsymbol{\sigma}\widehat{\mathbf{R}},\widehat{\sigma}_{ij}=\widehat{R}_{ri}\widehat{R}_{sj}\sigma_{rs} \tag{10.71}$$

$$\widehat{R}_{ij}(t)\equiv\mathbf{e}_i\cdot\widehat{\mathbf{e}}_j(t)\ (=\cos(\mathbf{e}_i,\widehat{\mathbf{e}}_j(t))) \tag{10.72}$$

$\widehat{\mathbf{e}}_i(t)$ are the base vectors taken to the directions of the principal axes of the orthotropic anisotropy. Needless to say, Eq. (10.70) is not a general tensor expression but is merely the expression by the components. The variation of $\widehat{\mathbf{e}}_i$ is calculated using the following equation with the initial value of $\widehat{\mathbf{e}}_{i0}$.

$$\widehat{\mathbf{e}}_i=\widehat{\mathbf{e}}_{i0}+\int\dot{\widehat{\mathbf{e}}}_i dt \tag{10.73}$$

where $\dot{\widehat{\mathbf{e}}}_i$ is given by

$$\dot{\widehat{\mathbf{e}}}_i = \boldsymbol{\omega}_a \widehat{\mathbf{e}}_i \, (\boldsymbol{\omega}_a = \dot{\widehat{\mathbf{e}}}_i \otimes \widehat{\mathbf{e}}_i) \tag{10.74}$$

Here, the stress rate $\dot{\widehat{\sigma}}_{ij}$ is given by

$$\dot{\widehat{\sigma}}_{ij} = \mathring{\widehat{\sigma}}_{ij} = \widehat{R}_{ri}\widehat{R}_{sj}\mathring{\sigma}_{rs} = \widehat{R}_{ri}\widehat{R}_{sj}(\dot{\sigma}_{rs} - \omega_{arp}\sigma_{ps} + \sigma_{rp}\omega_{aps}) \tag{10.75}$$

noting Eqs. (1.86) and (4.55) with $\mathbf{Q} = \widehat{\mathbf{R}}^T$.

Various anisotropic yield surfaces in the plane stress state are proposed by the Barlat's group (e.g. Barlat et al. 2007), Yoshida (2015), etc.

10.7 Representation of Isotropic Mises Yield Condition

The isotropic yield function described by Eq. (6.57) can be expressed in the following various forms.

$$\begin{aligned} f(\boldsymbol{\sigma}) = \sigma^{eq} &= \sqrt{\frac{3}{2}}\|\boldsymbol{\sigma}'\| = \sqrt{\frac{3}{2}}\sqrt{\sigma'_{rs}\sigma'_{rs}} \\ &= \sqrt{\frac{3}{2}}\sqrt{\sigma'^2_{11} + \sigma'^2_{22} + \sigma'^2_{33} + 2(\sigma'^2_{12} + \sigma'^2_{23} + \sigma'^2_{31})} \\ &= \sqrt{\frac{1}{2}}\sqrt{(\sigma_{11} - \sigma_{22})^2 + (\sigma_{22} - \sigma_{33})^2 + (\sigma_{33} - \sigma_{11})^2 + 6(\sigma^2_{12} + \sigma^2_{23} + \sigma^2_{31})} \\ &= \sqrt{\frac{3}{2}}\sqrt{\sigma'^2_1 + \sigma'^2_2 + \sigma'^2_3} \\ &= \sqrt{\frac{1}{2}}\sqrt{(\sigma_1 - \sigma_2)^2 + (\sigma_2 - \sigma_3)^2 + (\sigma_3 - \sigma_1)^2} = F \end{aligned} \tag{10.76}$$

The combined test of the tensile stress $\sigma(=\sigma_{11})$ and the distortional stress $\tau(=\sigma_{12})$ for a thin wall cylinder specimen is widely adopted for metal. In this case Eq. (10.76) is rewritten as

$$\sigma^2 + (\sqrt{3}\tau)^2 = F^2 \tag{10.77}$$

Then, the Mises yield condition is shown by a circle of radius F in the $(\sigma, \sqrt{3}\tau)$ plane.

The visualization of the stress state can be realized in the space of three and less dimension. The stress state can be represented completely in the principal stress space when principal stress directions are fixed to materials and only the principal stress values change. In general, however, one must use the six-dimensional space or memorize the variation of the principal stress direction if the directions change. However, in the cases for which the number of independent variable components is less than three, such as the tension-distortion test described above and the plane

stress and strain tests, the state of stress can be represented in the three and less dimensional stress space. The *Ilyushin's isotropic stress space* (Ilyushin 1963) is convenient to depict the Mises yield surface, which depends only on the deviatoric stress, as explained below.

The deviatoric stress tensor includes the five independent variables and thus the Mises yield surface in Eq. (10.76) is described by the independent components as follows:

$$f(\boldsymbol{\sigma}) = \sqrt{3\sigma_{11}'^2 + 3\sigma_{22}'^2 + 3\sigma_{11}'\sigma_{22}' + 3(\sigma_{12}' + \sigma_{23}'^2 + \sigma_{31}'^2)}$$
$$= \sqrt{\left(\frac{3}{2}\sigma_{11}'\right)^2 + 3\left(\frac{1}{2}\sigma_{11}' + \sigma_{22}'\right)^2 + 3(\sigma_{12}' + \sigma_{23}'^2 + \sigma_{31}'^2)} = F$$

and thus it can be rewritten as

$$S_1^2 + S_2^2 + S_3^2 + S_4^2 + S_5^2 = F^2 \tag{10.78}$$

in the five-dimensional space with the axes

$$S_1 = \frac{3}{2}\sigma_{11}',\ S_2 = \sqrt{3}\left(\frac{1}{2}\sigma_{11}' + \sigma_{22}'\right),\ S_3 = \sqrt{3}\sigma_{12}',\ S_4 = \sqrt{3}\sigma_{23}',\ S_5 = \sqrt{3}\sigma_{31}' \tag{10.79}$$

Equation (10.78) exhibits the *five-dimensional spherical super surface*. Further, consider the expression of the Mises yield surface for the plane stress and strain conditions in the following.

10.7.1 Plane Stress State

The plane stress state fulfilling $\sigma_{3j} = 0$ can be described in the three-dimensional space $(\sigma_{11}, \sigma_{22}, \sigma_{12})$ and thus the Mises yield condition (10.76) is described by the following equation.

$$\sqrt{\sigma_{11}^2 - \sigma_{11}\sigma_{22} + \sigma_{22}^2 + 3\sigma_{12}^2} = F \tag{10.80}$$

On the other hand, Eq. (10.80) can be described in the two-dimensional principal stress plane as follows:

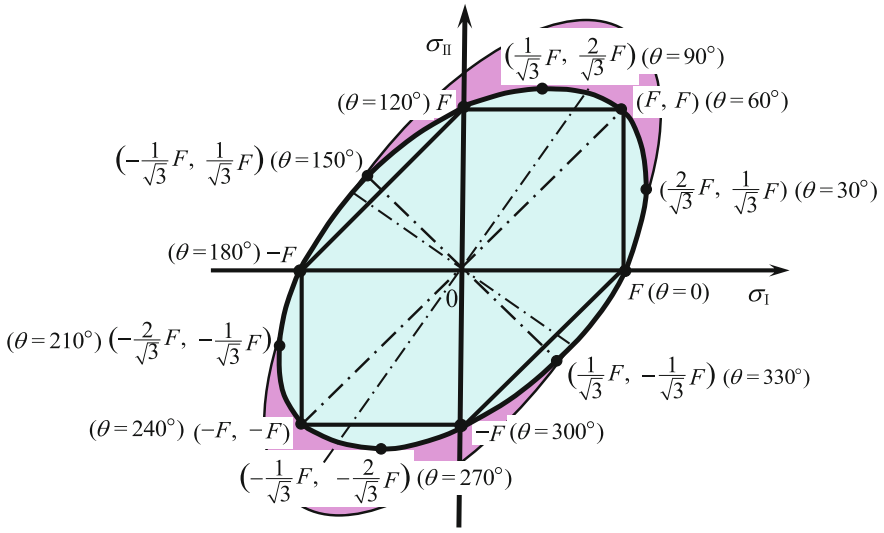

Fig. 10.18 Mises yield surface in the plane stress condition (Thin curve describes Hill's orthotropic Mises yield condition)

$$\sqrt{\sigma_1^2 - \sigma_1\sigma_2 + \sigma_2^2} = F \tag{10.81}$$

which is the section of the Mises yield condition cut by the plane $\sigma_3 = 0$ and exhibits *Mises's ellipse* in the principal stress plane (σ_1, σ_2) as shown in Fig. 10.18. It follows from the third equation of Eq. (1.264) that

$$\sigma_m = -\sqrt{\frac{2}{3}}\|\boldsymbol{\sigma}'\| F\cos\left(\theta + \frac{2}{3}\pi\right) = -\frac{2}{3}F\cos\left(\theta + \frac{2}{3}\pi\right) \tag{10.82}$$

because of $\sigma_m + \sigma_3' = 0$ leading to $\sigma_m = -\sigma_3'$. Substituting Eq. (1.264) and Eq. (10.82) with $\|\boldsymbol{\sigma}'\| = \sqrt{2/3}F$ into Eq. (1.260), one obtains

$$\left.\begin{aligned} \sigma_1 &= -\frac{2}{3}F\cos\left(\theta + \frac{2}{3}\pi\right) + \frac{2}{3}F\cos\theta = \frac{2}{\sqrt{3}}F\sin\left(\theta + \frac{\pi}{3}\right) \\ \sigma_2 &= -\frac{2}{3}F\cos\left(\theta + \frac{2}{3}\pi\right) + \frac{2}{3}F\cos\left(\theta - \frac{2}{3}\pi\right) = \frac{2}{\sqrt{3}}F\sin\theta \end{aligned}\right\} \tag{10.83}$$

from which the coordinates of main points on the Mises's ellipse are calculated as shown in Fig. 10.18. The thin curve shows the Hill's orthotropic Mises yield surface in Eq. (10.50), which is rotated the principal axes of ellipse with the changes of its long and short radii from the isotropic Mises yield surface.

Next, consider the *Ilyushin's isotropic stress space* in which the variables in Eq. (10.79) are used. Here, in the present case fulfilling $\sigma_{3j} = 0$ leading to $S_4 =$

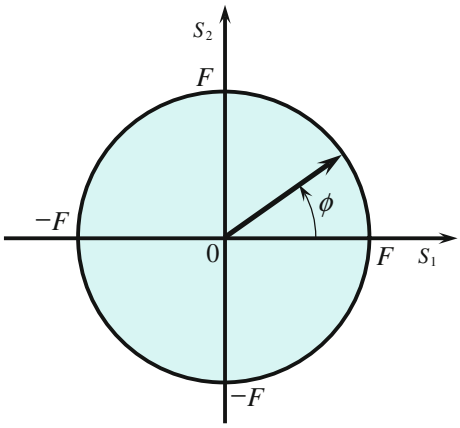

Fig. 10.19 Mises yield surface in plane stress state without shear stress

$S_5 = 0$ the Mises yield surface is represented by the sphere in the (S_1, S_2, S_3) space, while it holds that

$$\left.\begin{aligned} S_1 &= (3/2)\sigma'_{11} = (3/2)[\sigma_{11} - (\sigma_{11} + \sigma_{22})/3] = \sigma_{11} - \sigma_{22}/2 \\ S_2 &= \sqrt{3}[(1/2)\sigma'_{11} + \sigma'_{22}] \\ &= \sqrt{3}\{(1/2)[\sigma_{11} - (\sigma_{11} + \sigma_{22})/3] + [\sigma_{22} - (\sigma_{11} + \sigma_{22})/3]\} = (\sqrt{3}/2)\sigma_{22} \end{aligned}\right\} \tag{10.84}$$

Furthermore, in the case fulfilling $\sigma_{12} = 0$, the Mises yield surface is represented by the circle in the (S_1, S_2) plane (Fig. 10.19). Here, setting

$$S_1 = F\cos\phi, \quad S_2 = F\sin\phi \tag{10.85}$$

and substituting them into Eq. (10.84), it holds that

$$\sigma_{11} = \frac{2}{\sqrt{3}}F\ \sin\left(\phi + \frac{\pi}{3}\right), \quad \sigma_{22} = \frac{2}{\sqrt{3}}F\ \sin\phi \tag{10.86}$$

10.7.2 Plane Strain State

If the elastic strain rate can be ignored compared with the plastic strain rate in the plane strain state, the following relation holds by substituting $D^p_{33} = \dot{\lambda}\,\sigma'_{33} = 0$ into $\sigma'_{rr} = 0$.

$$\sigma_{33} = \frac{1}{2}(\sigma_{11} + \sigma_{22}) \tag{10.87}$$

Then, the Mises yield surface is described from Eq. (10.76)$_3$ by

$$\sqrt{3}\sqrt{\left(\frac{\sigma_{11} - \sigma_{22}}{2}\right)^2 + \sigma_{12}^2} = F \tag{10.88}$$

which is represented by the Mohr's circle in the plane of the normal and the shear stresses.

References

Barlat F, Yoon JW, Cazacu O (2007) On linear transformations of stress tensors for the description of plastic anisotropy. Int J Plast 23:876–896

Chaboche JL (1989) Constitutive equations for cyclic plasticity and cyclic viscoplasticity. Int J Plast 5:247–302

Chaboche JL (1991) On some modifications of kinematic hardening to improve the description of ratcheting effects. Int J Plast 7:661–678

Chaboche JL (2008) A review of some plasticity and viscoplasticity constitutive theories. Int J Plast 24:1642–1693

Chaboche JL, Dang-Van K, Cordier G (1979) Modelization of the strain memory effect on the cyclic hardening of 316 stainless steel, Transaction on 5th International Conference SMiRT, Berlin, Division L., Paper No. L. 11/3

Delobelle P, Robinet P, Bocher L (1995) Experimental study and phenomenological modelization of ratchet under uniaxial and biaxial loading on austenitic stainless steel. Int J Plast 11:295–330

Ellyin F (1997) Fracture damage, crack growth and life prediction. Chapman & Hall, London

Ellyin F, Xia Z (1989) A rate-independent constitutive model for transient non-proportional loading. J Mech Phys Solids 37:71–91

Ghaei A, Green DE (2010) Numerical implementation of Yoshida-Uemori two-surface plasticity model using a fully implicit integration scheme. Compt Mater Sci 48:195–205

Hashiguchi K (2015c) Cyclic stagnation of isotropic hardening in metals, In: Proceedings of 2nd Science Meeting of Kyushu Branch of Society Material Science, Japan, B18

Hashiguchi K, Ueno M (2017) Elastoplastic constitutive equation of metals under cyclic loading. Int J Eng Sci 111:86–112

Hashiguchi K, Ueno M, Ozaki T (2012) Elastoplastic model of metals with smooth elastic-plastic transition. Acta Mech 223:985–1013

Hashiguchi K, Yamakawa Y (2012) Introduction to finite strain theory for continuum elasto-plasticity, Wiley series in computational mechanics. Wiley, Chichester

Hassan T, Taleb T, Krishna S (2008) Influence of non-proportional loading on ratcheting responses and simulations by two recent cyclic plasticity models. Int J Plast 24:1863–1889

Higuchi R, Okamura K (2016) Prediction of residual stress change due to cyclic loading ~ validation of advantage of sub-loading surface model ~

Hill R (1948) Theory of yielding and plastic flow of anisotropic metals. Proc Royal Soc Lond A193:281–297

Hill R (1990) Constitutive modeling of orthotropic plasticity in sheet metals. J Mech Phys Solids 38:241–249

Ilyushin AA (1963) Plasticity—foundation of the general mathematical theory, Izdatielistbo Akademii Nauk CCCR (Publisher of the Russian Academy of Sciences), Moscow

Jiang Y, Zhang J (2008) Benchmark experiments and characteristic cyclic plasticity deformation. Int J Plast 24:1481–1515

Kobayashi M, Ohno N (2002) Implementation of cyclic plasticity models based on a general form of kinematic hardening. Int J Numer Meth Eng 53:2217–2238

Lee JY, Barlat F, Lee MG (2015) Constitutive and friction modeling for accurate springback analysis of advanced high strength steel sheets. Int J Pasticity 71:113–135

Lemaitre JA (1992) A course on damage mechanics. Springer, Heidelberg

Murakami S (2012) Continuum damage mechanics: a continuum mechanics approach to the analysis of damage and fracture. Springer, Dordrecht

Ohno N (1982) A constitutive model of cyclic plasticity with a non-hardening strain region. J Appl Mech (ASME) 49:721–727

Sun L, Wagoner RH (2011) Complex unloading behavior: nature of the deformation and its consistent constitutive representation. Int J Pasticity 27:1126–1144

Wagoner RH, Lim H, Lee MG (2013) Advanced issues in springback. Int J Pasticity 45:3–20

Xia Z, Ellyin F (1994) Biaxial ratcheting under strain or stress-controlled axial cycling with constant hoop stress. J Appl Mech (ASME) 61:422–428

Yoshida F, Uemori T (2002) A model of large-strain cyclic plasticity describing the Bauschinger effect and workhardening stagnation. Int J Plast 18:661–686

Yoshida F, Uemori T (2003) A model of large-strain cyclic plasticity and its application to springback simulation. Int J Mech Sci 45:1687–1702

Yoshida F, Hamasaki H, Uemori T (2015) Modeling of anisotropic hardening of sheet metals including description of the Bauschinger effect. Int J Plast 75:170–188